Development and Characterization of an *ex vivo* Organotypic Non-Small Cell Lung Cancer Model to Study the Effect of Elevated Oxygen Treatment

Joakim Hekland

This thesis is submitted in partial fulfilment of the requirements for the degree of Master in Biomedical Science

Department of Biomedicine
University of Bergen, Norway
May 2021

Acknowledgements

First, I want to give big thanks my supervisors Agnete Engelsen, Linda Stuhr and Maria Lie Lotsberg for giving me the opportunity to work with the exiting master project. Their support and knowledge have been essential during the whole project. Their support during the writing process as well as the IMC experiments has been elementary to complete the thesis in time.

I would also like to say thank to Jim, Sissel, Endre, Gerd and more of the staff at the Cellnet group for the essential help. Additionally, a thank you to Maria Ramnefjell at Dept. Pathology, Marianne Aanerud, Fabian Gärtner and Pirjo Rijtta Salminen - the pulmonologists at Haukeland Universitets Sykehus, MIC and Jørn Skavland at the FLOW core facilities.

Finally, I would like to thank my girlfriend, roommates, and family for supporting my work and helping me to relax, when necessary, during these Covid-times!

Table of Contents

Abbreviations

abbreviation	term
AB-PAS	Alcian blue – periodic acid Schiff
CC3	cleaved caspase 3
CK5	cytokeratin 5
CK6	cytokeratin 6
CK7	cytokeratin 7
CyTOF	time-of-flight mass cytometry
ECM	extracellular matrix
EGFR	endothelial growth factor receptor
EMT	epithelial to mesenchymal transition
EMT-TF	epithelial to mesenchymal transition transcription factor
EMP	epithelial mesenchymal plasticity
FFPE	formalin-fixed paraffin-embedded
HE	hematoxylin and eosin
HIF	hypoxia induced factor
HRE	hypoxia responsive elements
IF	immunofluorescence
IMC	imaging mass cytometry
K8/18	keratin 8 & 18
LGR5	leucine-rich repeat-containing G-protein coupled receptor
LUAD	adenocarcinoma
LUSC	squamous cell carcinoma

MET	mesenchymal to endothelial transition
MSW	meter of sea water
NGS	next generation sequencing
NSCLC	non-small cell lung cancer
p40	tumor protein p40
p63	tumor protein p63
PD1	programed death receptor 1
PDL1	programmed death receptor ligand 1
p-Tyr	phosphotyrosine
RCF	relative centrifugal force
ROI	region of interest
RT	room temperature
RTK	receptor tyrosine kinase
SCLC	small cell lung cancer
STFPC	surfactant protein C
TKI	tyrosine kinase inhibitor
TNM	Tumor – Nodes - Metastasis
TRP63	tumor protein 63
tSNE	t-distributed stochastic neighbor embedding
VEGFA	vascular endothelial growth factor A

Summary

Lung cancer is a leading cause of cancer-related morbidity and mortality worldwide, and also the cancer-form responsible for most cancer related deaths in Norway. Non-small cell lung cancer (NSCLC) accounts for approximately 80% of the lung cancer cases. Owing to the introduction of targeted therapies and immune checkpoint inhibitors (ICI), the treatment of NSCLC has changed drastically in recent years, in particular due to the remarkable clinical efficacy of ICI observed in a subset of patients. **Although a minority of patients show prolonged clinical benefit of these drugs, innate and acquired resistance to ICI limit the clinical benefit and the complex molecular mechanisms mediating resistance is still poorly understood** Thus, there are a need for preclinical models which are representative for the heterogeneity of the tumor microenvironment.

3D patient organoids emerge as a unique and robust tool. This *in vitro* model mimics the biological *in vivo* characteristics of the primary patient tissue. Since hypoxia is pivotal for cancer growth and progression, we have aimed to study the effect of "the flip of the coin", namely hyperoxia. Furthermore, to get a better understanding of the complex communication between tumor and the stroma, we combinate the single cell high dimensional analysis technique, imaging mass cytometry with the organoid model.

The first two objectives of this thesis were to develop an organoid model from human non-small cell lung cancer resection specimens, and to characterize the histoarchitecture and cellular composition of the organoids compared to the malignant tumors they derive from. Six different tumor resection specimens of various histological subtypes of NSCLC´s was included in the study. Establishment of patient derived organoids were successful for all resection specimens. Comparison between tumor and derived organoid tissues, and between the individual organoids was performed through application of various staining techniques. Additionally, preservation of genetic abbreviations from patient tumor, detected by next generation sequencing (NGS), was elucidated by antibody staining in derived organoids. We were able to confirm that the histological characteristics of different patient derived organoids varied from patient to patient, as expected due to differences in histological subtypes among the tumors. Most importantly, the derived organoids show similar growth characteristics and cellular composition compared to the tumor of origin. Also, the genetic mutations detected in the tumor of origin was shown to be preserved in organoid tissues. Furthermore, the IMC data show variation of protein

expression between the adenocarcinoma and squamous cell carcinoma organoids. The cytokeratin, CK7, was shown to be expressed only in the adenocarcinoma derived organoids.

The final objective was to explore the effect of normobaric and hyperbaric oxygen treatment on cancer cell proliferation and phenotype, as well as ECM composition. Harvest of organoids in the elevated oxygen treatment groups was less efficient, indicating a suppressive effect of elevated oxygen. Reduced expression of the proliferation marker Ki67 were detected in the normobaric oxygen treatment group compared to control, however the hyperbaric oxygen treatment showed variable results. Thus, these experiments need to be repeated in order to be able to conclude about the efficiency of elevated oxygen therapy, but our results support further exploration of this experimental therapy in the newly established model.

1. Introduction

1.1 Cancer and Cancer Statistics

Cancer is a global problem and one of the leading causes of deaths. In 2020, the World Health Organization estimated that cancer caused close to 10 million annual deaths worldwide (1). Cancer is a huge global health problem, however low- to middle-income countries accounts for about 70% of cancer related deaths. Use of tobacco, intake of alcohol, unhealthy diet and physical inactivity are the 4 major risk factors for developing cancer, and 22% of all cancer deaths are due to tobacco use (1). Worldwide, cancer is expected to become the leading cause of death by the end of the 21st century (2). In Norway, as in many other high-income countries throughout the world, cancer already is the most lethal disease (3).

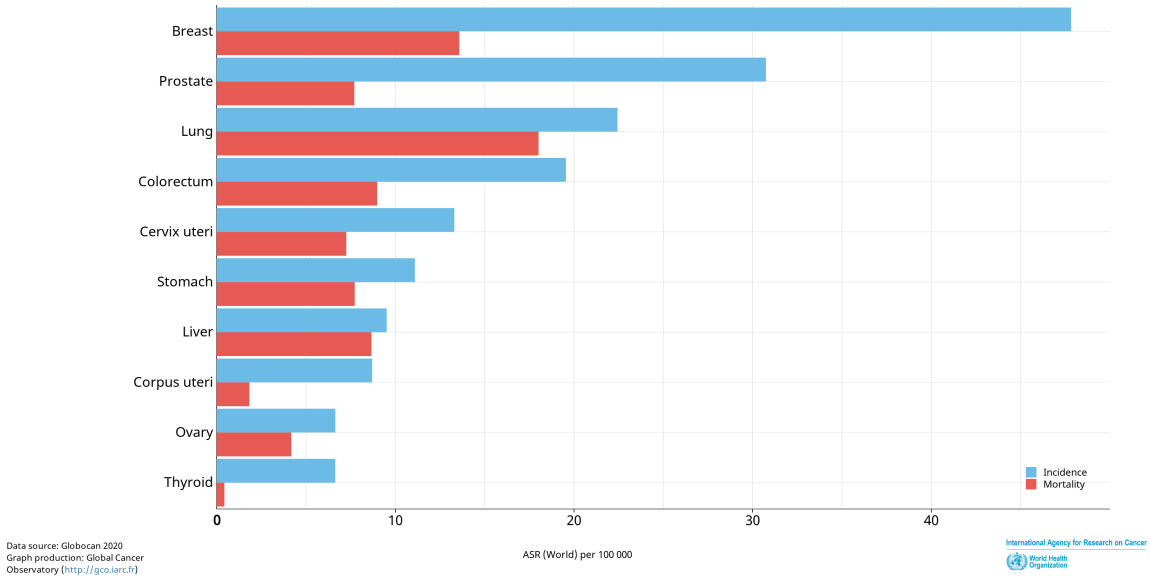

Figure 1.1: Estimated age-standardized incidence and mortality worldwide in 2020 by WHO. Both sexes combined, and all ages are included. Data source: Globocan 2020. Graph by Global Cancer observatory (4)

The best strategy to reduce cancer incidence is by reducing the risk factors mentioned above. Another strategy to lower the lethality rate is improved early detection, diagnosis, and onset of treatment, which could be achieved by raising awareness of symptoms, screening, and good access to medical services in general (1).

1.2 Lung Cancer and its Subtypes

Lung cancer accounts for nearly one quarter of all cancer related deaths. This malignancy has clearly the highest death rate of all cancer throughout the world due to the combination of its incidence and mortality rates, with an estimated survival rate of only 17.8% after 5 years. It is also the most common sex independent malignancy (Figure 1.1) (5, 6).

Lung cancer is divided into two major types. Non-small cell lung cancer (NSCLC) is the dominant type of lung cancer, and it accounts for 80 – 85% of all cases of lung cancer. The second major type of lung cancer is small-cell lung cancer (SCLC), which constitutes the remaining 15 – 20% of lung cancer cases (7). SCLC has the most aggressive growth of all lung cancers, with a median survival time of just two to four months (8). Nevertheless, NSCLC is not as aggressive but due to the high incidence rate, improvement of treatment strategy as well as the clinical outcome is urgently needed. Due to the severity of lung cancer at large, both for SCLC and NSCLC it is important to search for new therapeutic strategies to improve the clinical outcome (7). One of the aims of the present thesis is to test a new therapeutic strategy for NSCLC.

NSCLC is divided into three major subtypes, adenocarcinoma, squamous cell carcinoma and large cell anaplastic carcinoma. Adenocarcinoma accounts for approximately 40% of all lung cancer cases, while squamous cell carcinoma represents around 25% - 30% and large cell anaplastic carcinoma with roughly 10% of the total lung cancer cases (9), the rest are SCLC cases. The cellular origin of lung cancer is still unknown for most cases. However, adenocarcinomas are usually believed to origin from the distal alveolar cells located in the alveolar lung epithelia, while squamous cell carcinoma traditionally is thought to arise from cells residing in the more proximal airway tissue. Tissue stem cells are often believed to be the cell of origin for malignancies due to their long life span which allows for increased chances of accumulation of mutations and initiation of tumorigenesis (10).

1.3 The TNM staging of non-small cell lung cancer (NSCLC)

The stage classification system of NSCLC is based on the TNM-system, developed by the International Association for the staging of Lung Cancer (IASLC). In the TNM-system T stands for tumor, N stands for nodes and M stands for metastasis. In this system, stage is defined by the extent of the size of the primary tumor, the extent of spread to regional lymph nodes in addition to metastasis to distal sites. No other factors such as the biological characterization of the tumor or clinically symptoms are included in this stage classification system (11). For now, the staging system remains the most important prognostic factor for survival rates and time, despite the huge efforts of research in the area of additional molecular prognostic factors. In the future we will most likely see the development of a system combining the TNM-system and biomarkers (12).

The stage classification TNM system is divided into four major stages, stage I, II, III and IV as shown in Table 1.1. These stages are further split into individual substages. The staging system is rather complex, and each stage is determined by the composition of the TNM factors. In stage I, no spread to the lymph nodes nor distant metastasis have been detected. This means that N and M values equals 0, but values of T are higher than 0. For stages II and III, no metastasis has been detected, but most of the subtypes have spread to the lymph nodes. This means that in most substages N values exceeds 0, but the M value still equals 0. All cases in which there are metastasis, meaning that the M value exceeds 0, are classified as a stage IV malignancy, despite the values of T and N (12, 13).

Table 1.1 NSCLC stage classification TNM system.

Stage	T (Tumor size in cm)	N (Nodes)	M (Distant metastasis)
I	<3	0	0
II	3-7	>0	0
III	>7	>0	0
IV	Any	Any	>0

1.4 Treatment of NSCLC

When it comes to treatment of NSCLC patients it varies, but there are some standard recommendations for treatment based on the individual stages. For stage I malignancies in general the preferred treatment strategy is surgery. More specifically lobectomy is the recommended surgical procedure. Only selected patients presenting with stage I malignancies gets additional, or adjuvant, treatments. The recommendation for stage II malignancies is multidisciplinary treatment strategies, such as surgery followed by adjuvant platinum-based chemotherapy. Some stage II patients are candidates of chemo-radiotherapy treatments. For patients presenting with the more advanced stage III and IV cancers, the treatments are more individually tailored to the various substages and molecular features. Different multidisciplinary treatment strategies can include lymph node dissection, adjuvant chemotherapy and platinum-based chemo radiation therapy or immunotherapy with immune checkpoint inhibitors (14, 15).

The pathologist also evaluate the invasive probability of adenocarcinomas and classify them into five different predominant patterns, lepidic-, papillary-, acinar-, micropapillary- and solid adenocarcinoma (16). Molecular evaluation of the adenocarcinomas by next generation sequencing (NGS) and IHC-P is also performed. Patients positive for selective mutations, such as EGFR deletion in chromosome 19 are candidates for targeted therapy. Tyrosine kinase inhibitors (TKI) like erlotinib are suited for targeting cancer cells harboring this EGFR mutation (17). Each molecular aberration detected of the ones that are screened is suited for different target therapies (18).

In cases of squamous cell carcinomas on the other hand, NGS screening is not conducted. There are only a few target mutations in this subtype of NSCLC (19). In Norway, there are no targeted therapies in the treatment of the squamous cell carcinoma patients (15).

1.5 The Tumor Microenvironment

Tumors are present as heterogenous tissues with malignant cells surrounded by a tumor microenvironment. The tumor microenvironment consists of fibroblasts, endothelial-, stromal, and immune cells in addition to the extracellular matrix (ECM) (Figure 1.2) (20). The ECM is composed mainly of proteoglycans and fibrous proteins, such as collagens, laminins, and fibronectins, which together provide the ECM with varied architecture as well as viscoelasticity. The ECM fill the majority of the interstitial space within a tissue (21). The tumor microenvironment is more acidic than normal tissue. The acidic conditions of the tumor microenvironment are due to a general increased glucose metabolism, which leads to H^+ production and excretion. The increased glucose metabolism (glycolysis) in combination with poor perfusion results in a more acidic environment (pH 6.5 – 6.9). The acidic environment may lead to cathepsin proteinase release and activity which is believed to be involved in local invasion and tissue remodeling (22). Hypoxic conditions are one of the key features of the tumor microenvironment, described in more detail later (1.6). Within the tumor microenvironment there is exchange of advanced information driven by growth factors, cytokines, chemokines, enzymes, and proteins. It is believed that the communication between the malignant cells and the tumor microenvironment is a key factor for cancer development (20).

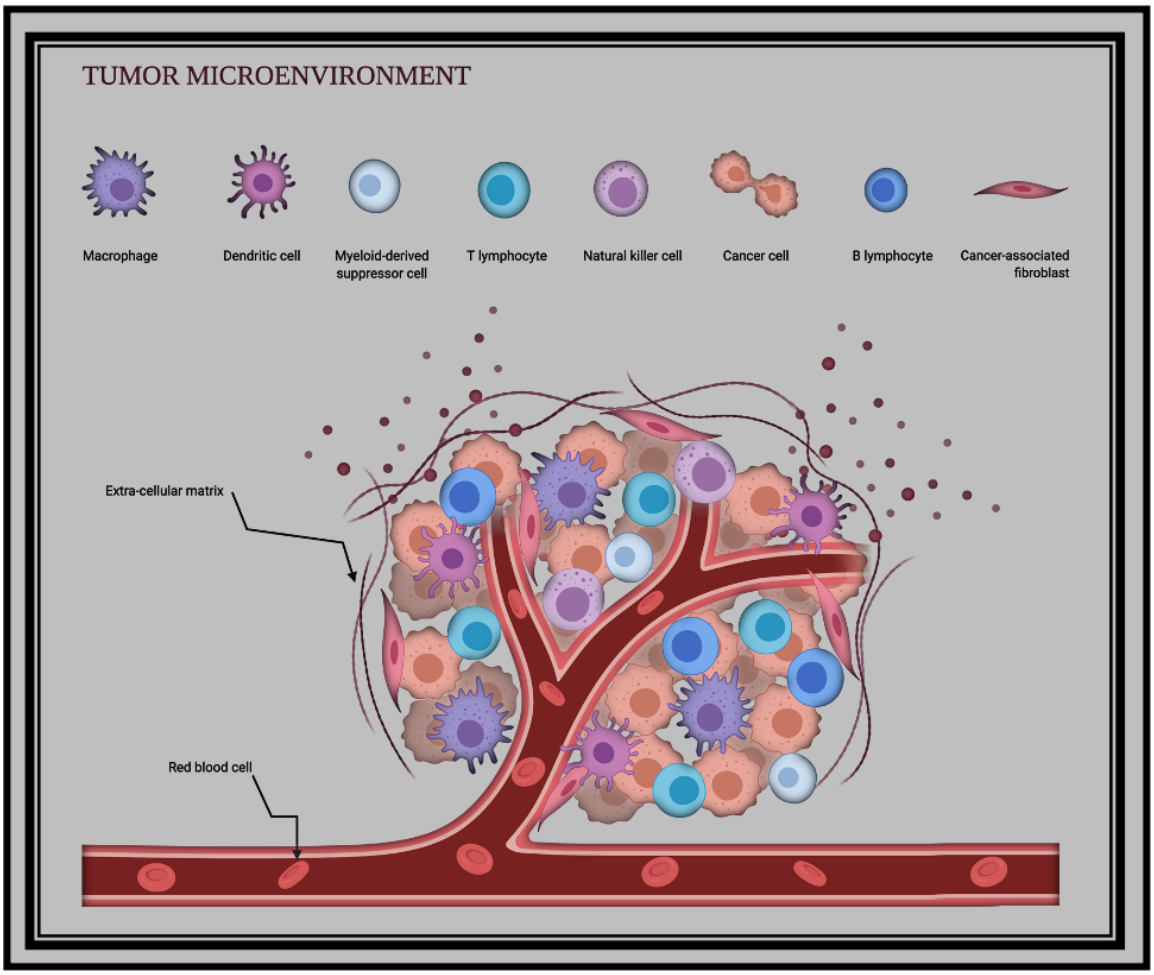

Figure 1.2: Illustration of the tumor microenvironment. The figure illustrates the basis structure of the tumor microenvironment, including extracellular matrix, and all the cellular components; fibroblasts, endothelial-, immune-, and cancer cells. Illustration made in Biorender.

1.6 Hypoxia in Cancer

Hypoxia is an important hallmark of the tumor microenvironment. Hypoxia is defined as an area where cells are deprived from the adequate amount of oxygen. Tumor hypoxia is recognized by the low levels of oxygen within the malignant tumor (0.3% - 2.1% O_2 (23)) (24), due to uncontainable proliferation, altered metabolism and abnormal tumor vessels.

Most solid tumors, including lung cancers, often consist of areas of acute or chronic hypoxia (25). Although severe and long-lasting hypoxia is toxic, many cancer cells have the ability to adapt to the hypoxic microenvironment, and are able to survive and proliferate despite the limited oxygen availability (26).

Conventionally, hypoxia was believed to be a limiting factor of tumor- and cancer growth, and this hypothesis was based on the fact that cells need oxygen for cell division. However, in the last decades hypoxia has been proven to be a key factor in cancer progression (27). Modern studies suggest that tumor hypoxia correlates with more malignant cancer cells (Figure 1.3) with induced cellular adaptions resulting in increased proliferation and cancer growth (15). It has been reported that hypoxia in tumors could result in improved oxidation and viability of malignant cells through induced angiogenesis, by increased glycolysis and up regulation of genes that are involved in cell survival and apoptosis and increased immune suppression (Figure 1.3) (28). In addition, hypoxia has been shown to induce epithelial to mesenchymal transition (EMT) which may lead to more therapy resistance and invasive and metastatic phenotypes (28, 29). Considering the latest research, hypoxia in tumor tissues can be seen as an independent prognostic factor and a significant risk factor of development of metastasis, in addition to development of treatment resistance (29).

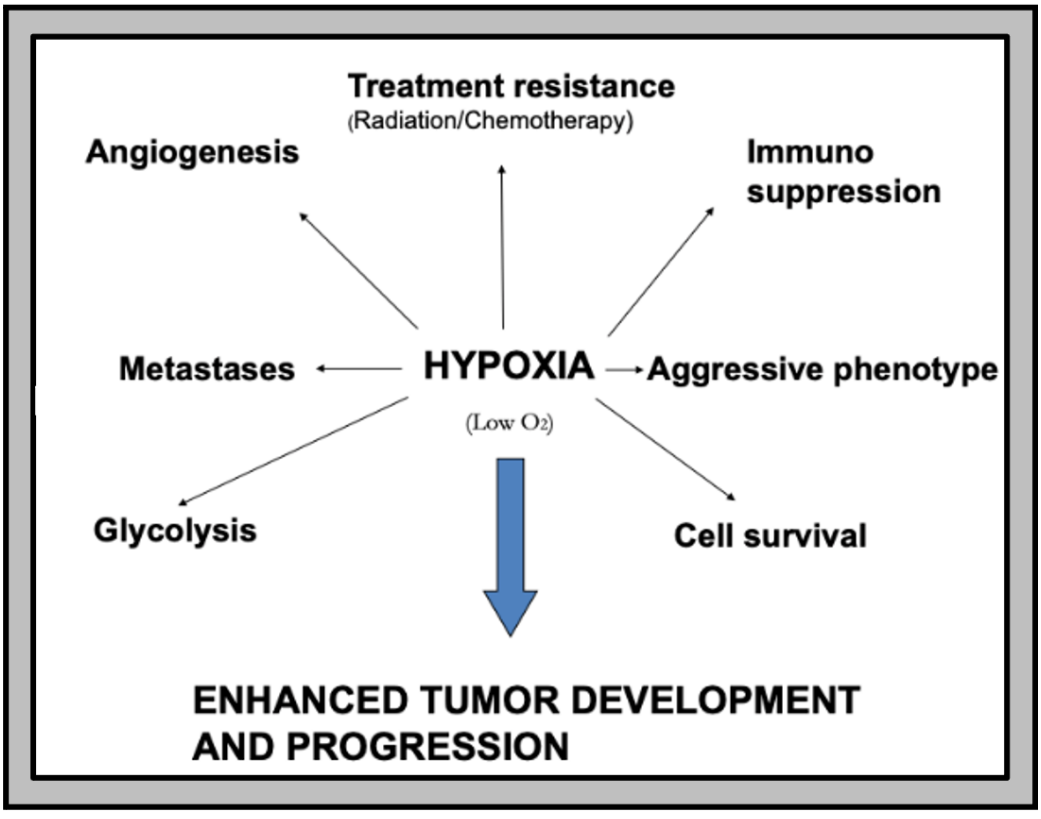

Figure 1.3: Tumor hypoxia results in enhanced tumor development and progression. This figure illustrates how hypoxia affects cancer. Hypoxia is involved in angiogenesis, immune suppression, cell survival and glycolysis and may result in metastases, an aggressive phenotype, and treatment resistance.

The effects of hypoxia are mediated by hypoxia-inducible factor (HIF) transcription factors. HIF1 alpha is the most enriched isoform of HIF, and this transcription factor responds to variation in available oxygen. HIF1 alpha is stabilized under hypoxic conditions. This increased expression is mostly controlled by decreased proteolytic degradation. Under these hypoxic conditions HIF1 alpha will translocate into the nucleus to communicate with genes to induce transcription of genes whose promoter is under regulation of hypoxia responsive elements (HREs). On the other hand normoxia rest destabilize HIF1 alpha by hydroxylation which ultimately results in degradation (Figure 1.4) (30). High expression of HIF1 alpha is found in a broad range of tumors, including NSCLC, and this hypoxia biomarker is associated with poor prognosis (31). HIF1 alpha is therefore an interesting therapeutic target.

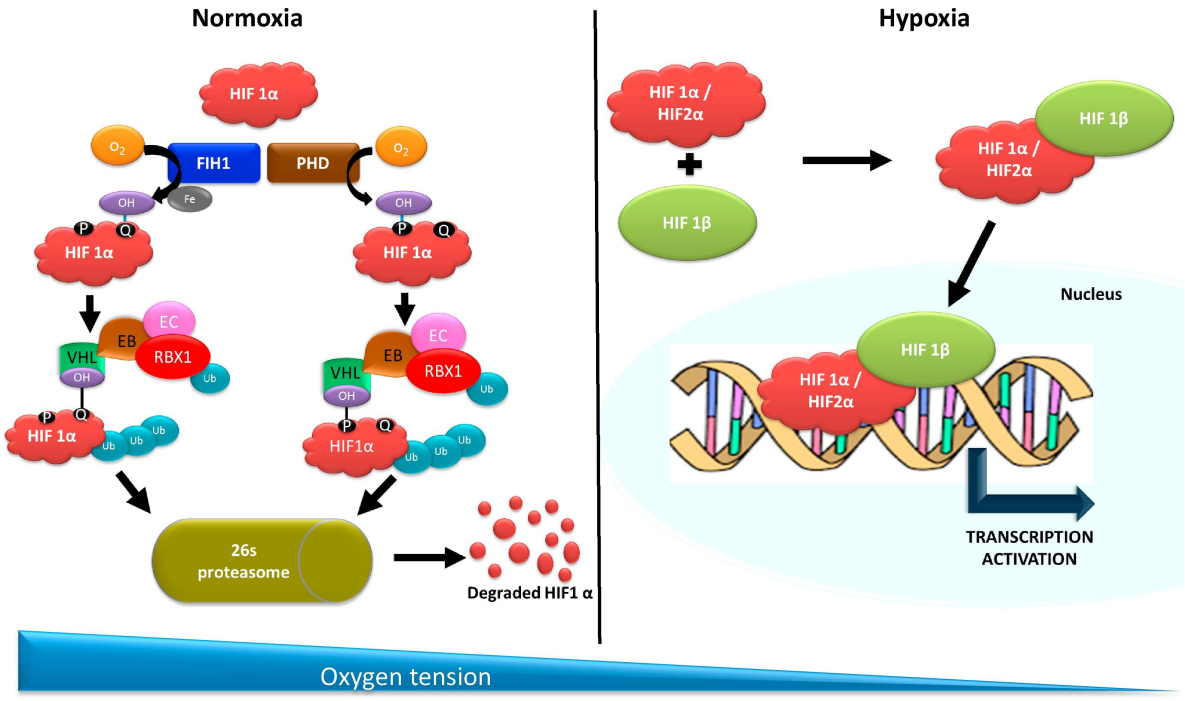

Figure 1.4: The role of HIF1 alpha in hypoxia and the degradation under normoxia.
Representation of how HIF1 alpha enters nucleus and activate transcription, and the mechanics of the degradation. Adapted from (32).

1.7 Epithelial to mesenchymal transition (EMT)

Despite the fact that heterogeneity of the origin and complex molecular mechanisms behind the development of malignancies are not fully known, and despite the heterogeneity, most solid tumors are established in similar manners. Cancer development is defined as a multistep process where somatic cells are first affected by an initiating step (*e.g*. predisposing environmental changes and epigenetic events) before promoting events like genetic mutations (33). The outcome of both events results in genetic modification. Accumulating somatic mutations mostly affects several hallmarks such as genomic instability, proliferative signaling, resisting of apoptosis, inflammation, angiogenesis, invasion, and metastasis (20).

Epithelial to mesenchymal transition (EMT) play an important role in cancer- development and progression. Traditionally, EMT is described as the transition of epithelial cells to cells with mesenchymal phenotype in the process of embryonic development. In this process the epithelial cells lose their polarity and cell to cell adhesion and become a more mesenchymal like cell type. This feature gives the malignant cells the opportunity of metastasis through multiple steps, including detachment of malignant cells from the primary tumor. This leads to invasion into the surrounding microenvironment, invasion into blood- and lymph vessels and finally, growth possibilities at a secondary site (mesenchymal to epithelial transition). Typical markers for EMT are vimentin, E-cadherin, upregulation of SNAIL, TWIST, TGF-beta, HIF1 alpha. However, some of these markers get upregulated, while others are downregulated during EMT. Importantly, EMT is not considered as a stochastic transition from completely epithelial to completely mesenchymal cells, but the cells can also undergo partial EMT to obtain intermediate E-M states. Together with the reversed mechanism, mesenchymal to epithelial transition (MET), this gives rise to Epithelial mesenchymal plasticity (EMP) which contributes to the cells ability to undergo functional adaption to the environment (34). The complexity of EMP ensures the malignant cells the property of adaption to the hostile and changing environment (35, 36).

The cancer progression could be driven by EMT-activating transcription factors (EMT-TFs). EMT-TF´s such as SNAIL1, SNAIL2 and TWIST1 have been proven to be partially or independently responsible for EMT. The EMT-TFs have a role in both cancer- progression, tumor growth, invasion, and metastasis. Additionally, these EMT-TFs have shown to acquire the ECM properties that promotes tumor growth (35).

1.8 The role of hypoxia in EMT

EMT is induced by hypoxia by HIF1alpha upregulation of the EMT-TFs which further activates EMT signaling pathways. The regulation is driven by the HIF´s. HIF1 alpha has been shown to promote EMT both trough upregulation of EMT-TFs like SNAI1- and TWIST (32). These mechanisms promote cancer progression and metastasis of malignant cells. HIF1 alpha is also correlated with the Cadherin switch (32), upregulation of N-Cadherin and downregulation of E-Cadherin (37), a key hallmark of EMT. Activation of AXL, a Receptor Tyrosine Kinase (RTK) has shown to be induced by HIF1 alpha. AXL is related to both EMT, tumor plasticity and drug resistance. The targeting of AXL by HIF1 alpha is regulated by the mentioned EMT-TFs as well as other microenvironmental factors (24). AXL are also directly regulated by hypoxia through a hypoxia responsive element (HRE) in its promoter.

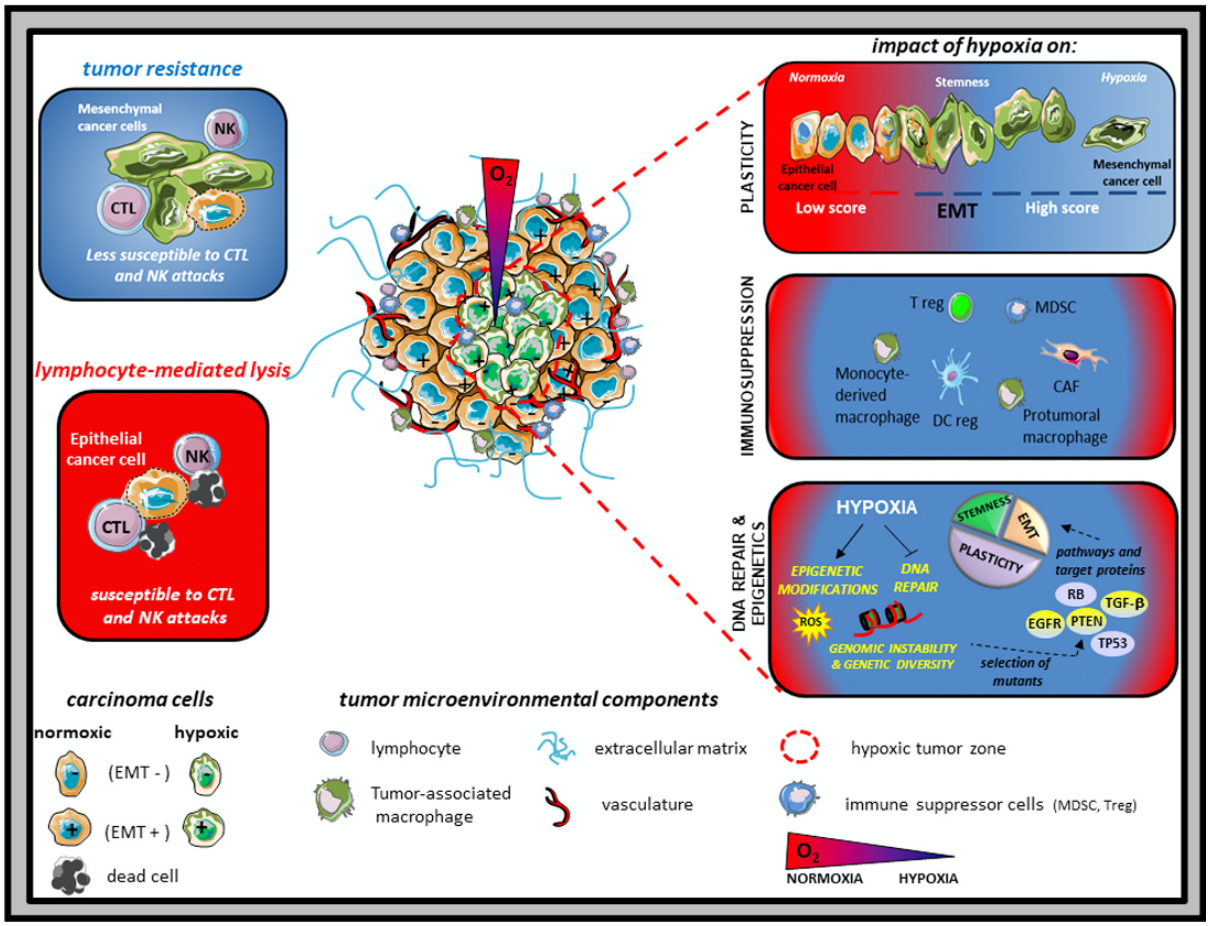

Figure 1.5: Hypoxia induced endothelial to mesenchymal transition. This illustration shows how hypoxia induces both EMT and immunosuppression as well as genetic and epigenetic changes in the tumor microenvironment. Illustration adapted from (24).

Thus, since hypoxia is pivotal for cancer growth and progression, one of the aims of this thesis is to evaluate the effect of elevated oxygen ("the flip of the coin") in a patient derived three-dimensional tumor organoid model.

1.9 Patient derived three-dimensional organoids

Patient derived organoids are three-dimensional cellular structures derived from either normal or tumor tissue. The stem cells have the capacity of self-forming into cellular structures resembling the tissue of origin (38), with both histopathology and gene mutations as the tissues they are derived from (32).

These organoids constitute a valuable research model for therapeutic efficacy, molecular mechanisms of drug resistance as well as toxic side-effects (33). We therefore developed patient derived NSCLC organoids to evaluate the effect of enhanced oxygen as a possible treatment modality.

2. Aims

Overall aim: Development and Characterization of an *ex vivo* Organotypic Non-Small Cell Lung Cancer Model to Study the Effect of Elevated Oxygen Treatment

Specific Aims:

1. **Establish an organoid model from human non-small cell lung cancer resection specimens.**

2. **Characterize the histoarchitecture and cellular composition of the organoids compared to the malignant tumors they derive from.**

3. **Explore the effect of normobaric and hyperbaric oxygen treatment on cancer cell proliferation and phenotype, as well as ECM components**

3. Methods

3.1 Establishment of a patient derived Organoid Model

For establishment of a patient derived lung tumor organoid model the protocol developed by Hans Clevers group (39) was used as a basis. We established organoids from a total of 6 patients Table 3.1. Out of the six tumor tissues received there were four adenocarcinomas (L1, L2, L3 and L5) and two squamous cell carcinomas (L4 and L6). Organoids derived from the individual patients were cultured for a varied time, from two to fourteen weeks. Most of the derived organoids was cryopreserved and harvested for future use, after two to three passages.

Table 3.1: Received tumor resection specimens for establishment of organoids.

Lung tumors	L1	L2	L3	L4	L5	L6
Type	LUAD	Lepidic LUAD	LUAD	LUSC	LUAD	LUSC

Table shows the six different lung tumor resection specimens received for establishment of derived organoids. Lung tumor 1-6 (L1-L6) and subtype of NSCLC. Establishment of NSCLC organoid cultures were successful for tissue from all lung tumor tissues included. LUAD – Adenocarcinoma and LUSD – Squamous cell carcinoma

For the establishment of organoids, tumor tissue specimen was received directly from the operating theatre at Haukeland Universitets Sykehus, or cryopreserved organoids received from Laurence Hoareau (researcher, Klinisk Institutt UiB). Both received tumor tissue and cryopreserved organoid were of NSCLC origin. All tumor tissues received was approved with informed consent with the individual patients, and all necessary documents was signed, and the study approved by the local ethical committee (REK Vest: #66610). The tumor tissue was brought to the cell lab where it was processed as described in Figure 4.1. Shortly described, the tumor resection specimen received directly from the operating theatre was minced into very

small pieces by scalpel, washed, digested in collagenase in an orbital shaker, strained and finally seeded in Matrigel-drops and cultured in defined serum-free medium.

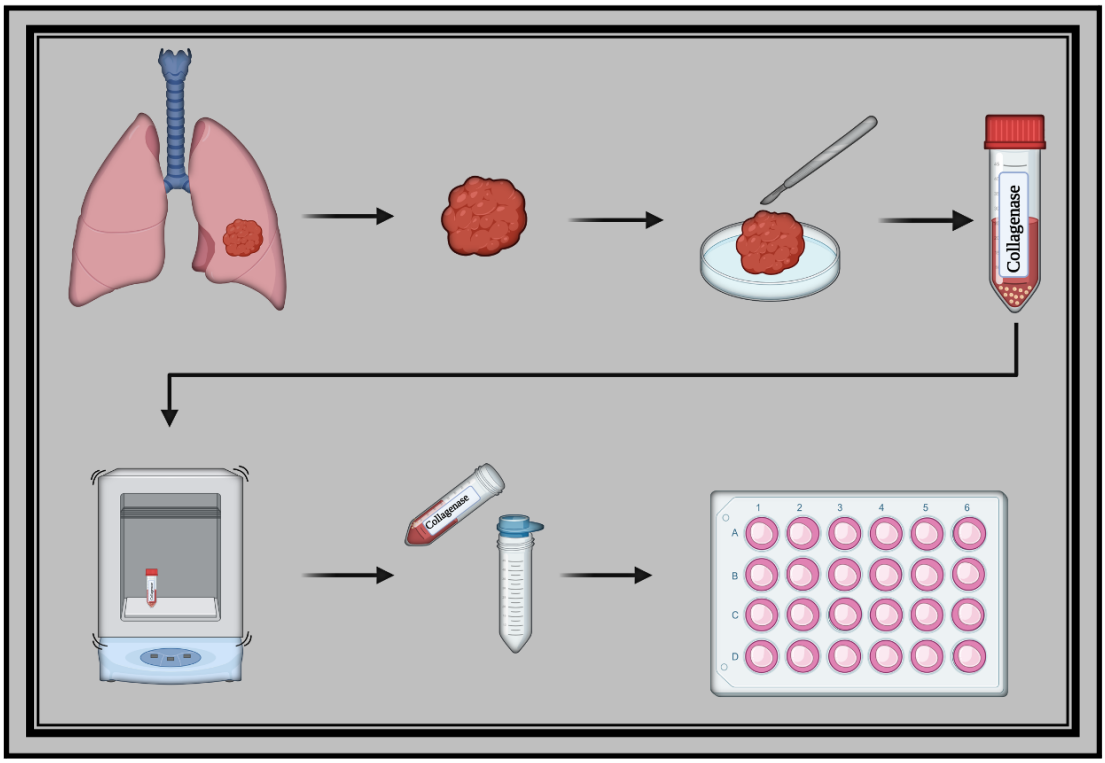

Figure 4.1: Establishment of patient derived lung tumor organoids workflow. This figure illustrates the roughly workflow of the establishment protocol used for the organoids. A tumor resection specimen received directly from the operating theatre was minced into very small pieces by scalpel, washed, digested in collagenase in an orbital shaker, strained and finally seeded in Matrigel-drops and cultured in defined serum-free medium. Illustration made in Biorender.

3.1.1 Protocol for establishment of patient-derived airway organoids

The organoids from lung patient number 1 (L1) were established from cryopreserved lung organoids of non-small cell lung cancer tissue (NSCLC). Cryopreserved organoids were thawed on ice and washed with AdDF^{+++} (Advanced DMEM/F12 with 1% GlutaMax, 10 mM HEPES and 1% Penicillin Streptomycin), and then spun down for 5 minutes at 400 RCF (relative centrifugal force). Washed organoids were resuspended in Matrigel (Corning, 354230, Bedford, MA, United States), 50 µL of Matrigel/well of organoid seeding. The resuspended organoids were seeded in each well, in pre warmed 24-well plates (Sarstedt, 83.3922, Newton, NC, United

States), before a 30-minute inverted incubation (upside down incubation of plate) at 37°C 5% O_2 and 5% CO_2, to ensure that the organoid do not sink to the bottom of the plate. Each of the wells will then establish a Matrigel dome. Organoids were cultured in two different conditions: differentiation medium with alveolar adapted conditions (Table1: Alveolar medium- as is, but with 3 µM of CHIR99021(GSK3 inhibitor/Wnt activator added), or with bronchiolar adapted conditions (Table1: Bronchiolar medium- as is). At the top of each of the Matrigel domes, 600 µL of the bronchiolar and/or alveolar differentiated medium was added. The organoid medium was changed twice a week and the organoids where passaged every other week.

The organoids from patient number 2 to 6 (L2 – L6) were established from patient lung tumor tissue. The resected tumor specimen was digested in Bronchiolar medium containing 1-2 mg/mL collagenase III (Worthington, #LS004182, Lakewood, NJ, United States). The seeding procedure was conducted as explained above for patient 1.

Table 1: Organoid medium as fundament medium.

Media component	**Signaling pathway**		**Supplier**	**Catalogue number**	**Final concentration**
	activation	block			
R-Spondin 1	Wnt/□-catenin signaling		Peprotech	120-38	500 ng/ml
FGF 7	FGFR2b signaling		Peprotech	100-19	25 ng/ml
FGF 10	FGFR2b signaling		Peprotech	100-26	100 ng/ml
Noggin	TGF-□ signaling		Peprotech	120-10C	100 ng/ml
A83-01	TGF-□ signaling		Tocris	2939	500 nM
Y-27632	ROCK signaling		Abmole	Y-27632	5 □M
SB202190	p38 MAPK signaling		Sigma	S7067	500 nM
B27 supplement	Insulin signaling		Gibco	17504-44	1x
N-Acetylcysteine	Antioxidant		Sigma	A9165-5g	1.25 mM
Nicotinamide	Co-enzyme precursor		Sigma	N0636	5 mM
GlutaMax 100x	Nutrient		Invitrogen	12634-034	1x
HEPES	Buffer		Invitrogen	15630-056	10 mM
Penicillin / Streptomycin	Antibiotics		Invitrogen	15140-122	100 U/ml 100 □g/ml
Amphotericin	Antibiotic/antimycotic		Sigma	A2942	2,5 µg/mL
Advanced DMEM/F12	Base medium		Invitrogen	12634-034	1x

Bronchiolar differentiation medium as in table. Alveolar differentiation medium as in table shown with added CHIR99021 (GSK3 inhibitor/Wnt activator), final concentration 3 µM.

3.1.2 Passage and expanding of airway organoids

Dense organoids for expanding were resuspended in cold $AdDF^{+++}$ and mechanically shared by using a pipette (pipetting up and down to Matrigel is dissolved) followed by centrifugation for 5 minutes at 400 RCF. Organoids were then resuspended in TrypLE (Gibco, 12604013, Grand Island, NY, United States) for 1-5 minutes before the addition of 10 mL $AdDF^{+++}$ for inactivation of TrypLE. A second spin down was executed, and the shared organoids were resuspended in Matrigel and reseeded to 24-well plates at a 1:6 ratio. Finally, appropriate medium (bronchiolar- or alveolar- medium) was added to the respectively organoids. For the less dense organoids or organoids for further experiments, the TrypLE step was skipped, and these organoids were reseeded in a 1:3 ratio.

3.1.3 Cryopreservation and fixation of airway organoids

For cryopreservation, the organoids were resuspended in wash medium (DMEM/F12 with 1% BSA cell culture grade) and centrifuged for 5 minutes at 400 RCF before the supernatant was discarded and the organoid pellet was resuspended in freeze medium (Bambanker Direct, BBD01, Düren, Germany). Harvesting of organoids was performed by resuspending in wash medium, spinning down at 400 RCF for 5 minutes, and washing organoids in PBS. Finally, organoids for FFPE embedding where fixed in 3,7% formalin.

3.1.4 Cell cultures

The lung cells HCC827 (ATCC, CRL-2868, Manassas, VA, United States) and A549 (ATCC, CCL-185) were used to generate control spheroids. The spheroids were used as control in the treatment of organoids, by comparing the impact of O_2 treatment between spheroids and organoids. HCC827 cells were cultured in RPMI 1640 medium (Sigma- Aldrich, R8758, Saint Louis, MO, United States) and A549 cells were cultured in DMEM F-12 Ham (Sigma Aldrich, D8062). Both mediums were supplemented with 2% L-Glutamine (Sigma Aldrich, #G-0781),

5% foetal bovine serum (FBS) (Gibco) and 1x concentration of 100 µg/µl streptomycin (Sigma Aldrich, Penicillin-Streptomycin, #P-0781).

3.1.5 Passaging of cells

Cells were split twice a week by first removing the medium and rinsing with PBS followed by the addition of 3 mL of trypsin and incubation at 37°C until the cells detached from the culture plate of the T-175 cell culture flask (Sarstedt, 83.3912.002). Cells were transferred to falcon tubes and spined down at 300 RCF for 5 minutes. Furthermore, the cells were resuspended in RPMI 1640 (HCC827) or DMEM F-12 Ham (A549) medium and seeded in new flasks.

3.1.6 Establishment of spheroids

Spheroids for IMC panel optimalisation were established from both HCC827 parental- and A549 cells. After trypsinization and collection of cells at centrifugation at 300 RCF for 5 minutes, the cells were resuspended in adequate medium (RPMI 1640 for HCC827 parental- and DMEM F-12 Ham for A549 cells) and counted by using Bürker counting chamber (Brand, 718920, Wertheim, Germany). To develop each spheroid, nine thousand cells in 100 µL of culture medium was seeded into each well of a round bottom ultra-low attachment 96 well-plate (Corning, 7007). Furthermore, the plate was centrifuged at 1000 RCF for 20 minutes. Addition of 100 µL of medium (as mentioned above) 3-4 days after the establishment was performed.

3.2 Characterization of organoids

3.2.1 Paraffin embedding of formalin fixed organoids

Harvested organoids were fixed in 3.7% formalin for 24 hours on a rotator (Stuart, SB3, Essex, UK) at room temperature. Organoids were then washed with PBS and stained with methylene green (40) for 5 minutes, before a second PBS wash. Further, organoids were resuspended in 100 µL of pre-warmed 1.5% agarose (Sigma, A9045) dissolved in TBS (Biorad, #1706435),

spun down at 100 RCF for 1 minute and incubated at 4°C for 30 minutes for solidification. The solid agarose pellet with organoids was transferred to a cell safe biopsy capsule (CellPath, EBE-0201-02A, UK and Simport, M498-2, Canada) and stored in 70% ethanol until paraffin embedding according to standard protocols. The paraffin embedded organoid specimens were sectioned by a microtome into 5 μm sections at the MIC core facility and collected at SuperFrost+ slides (10149870, Thermo Scientific). Hematoxylin and Eosin (HE) staining of each sample was performed. Both sectioning and staining procedures were performed by the Molecular Imaging Centre at the University of Bergen.

3.2.2 Immunofluorescent (IF) for confocal microscopy

Formalin fixed paraffin embedded slides were pencil labeled and deparaffinized from xylene (first for 5 minutes, then an additionally 10 minutes) trough decreasing levels of ethanol (100% x2, 96% x2, 70% x1 and 50% x1) followed by rehydration in H_2O. Performed for 5 minutes at each step. Heat-induced retrieval was performed in a decloaking chamber (Decloaking Chamber NxGen, Biocare Medical). The decloaking chamber was set to 95°C. The heat-induced epitope retrieval was conducted in DAKO Target Retrieval Solution (Dako, s1699) for 25 minutes. After the retrieval the chamber was cooled down to 80°C before the container with buffer and slides was incubated in room temperature for 20 minutes to cool down. Further, slides were washed in H_2O 3 x 5 minutes. Remaining water was wiped off and the tissue was encircled with a hydrophobic pen (DAKO, S2002, Glostrup, Denmark). Blocking buffer (TBST with 1% BSA) was added to the tissue for 30 minutes. Subsequently, the primary antibody incubation was conducted in 4°C, overnight. Primary antibody solution contains antibodies dissolved in blocking solution (Table 2).

Table 2: IF Primary antibodies. Primary antibodies used for IF.

Target	Host animal	Clone	Suplier	Cat#	Dilution	Comments
Alpha Tubulin	Mouse	DM1A	Sigma	T6199	1:200	Good
Ki67	Rabbit	poly	Abcam	ab15580	1:600	Good
CC3	Rabbit	poly	CST	9661S	1:100	Some signal
VEGFA	Rabbit	EP1215Y	Abcam	ab210073	1:100	Good
HIF-1alpha	Rabbit	EP1176Y	Abcam	ab185238	1:100	Good
panKeratin	Mouse	AE1/AE3	Dako	M3515	1:200	Good
AXL	Mouse	108724	CST	MAB154	1:100	Good

The next day the slides were moved out of the cold room. After 30 minutes calibration at room temperature, the slides where washed 3x5 minutes with PBS containing 0.1% Triton X-100 (Sigma, T8787), followed by secondary antibody in a 1:200 dilution incubation for 1 hour in room temperature. The secondary antibody solution consists of antibodies dissolved in blocking buffer (Table 3).

Table 3: IF Secondary Antibodies

Host	Target	Conjugate	Vendor	Cat#	Dilution
Goat	Rabbit	AF 647	Invitrogen	A21244	1:200
Goat	Mouse	AF 546	Invitrogen	A11030	1:200

The secondary antibodies were spun down before use, two different secondary antibodies were used to match the primary antibodies. After the secondary antibody incubation, the slides where washed 3x5 minutes in PBS. Finally, slides where mounted with Prolong DAPI Diamond (Thermo Fisher Scientific, P36962) and incubated over night at room temperature and moved to 4°C the next day.

3.2.3 Imaging by Olympus VS120 slide scanner

Samples with Hematoxylin and Eosin (HE) stains, and samples stained with fluorescent secondary antibodies were imaged and scanned using an Olympus VS120 slide scanner. For HE stained samples the Brightfield – Expert mode was used. Initially the samples were scanned with the overview option (4X). Followed by the overview scan, ROIs (region of interest) were selected and scanned using 20X objective. The ROIs were extracted and saved as JPEG (digital

image format). Samples stained with fluorescent secondary antibodies were imaged and scanned in the Fluorescent – Expert mode. Brightfield option was used in overview scan. After the overview scan, ROIs were selected and scanned with 20X objective with appropriate lasers. The laser intensity of each channel was adjusted against a negative control, and the laser intensity remained constant for the entire sample set. The ROIs (digital images) were extracted and saved as both JPEG and TIFF formats.

3.2.4 Quantification of Ki67 from IF data

For the immunofluorescent stained samples with Ki67 antibody (proliferation marker), mitotic index was evaluated in CellProfiler software (Broad Institute Inc., v.4.0.4). Firstly, TIFF files exported from Olympus VS120 was uploaded to Fiji (Fiji contributors) (41), where the TIFF files were split to the separate channels of DAPI (Nuclei) and Ki67. The sets of images were then uploaded into CellProfiler (42) and listed into two separate lists in the NamesAndTypes module. The DAPI images were scaled for visibility into a "DNA" image, while the Ki67 images were scaled for visibility into a "Ki67" image. The nuclei were identified by the IdentifyPrimaryObjects module, "DNA" image was used as input. Ki67 positive nuclei were identified in the same module using "Ki67" as input image. These two image sets were related in the RelateObjects module, with nuclei as parent- and Ki67 as child- object. After the two image sets were related, "Nuclei" was filtered by "Ki67" in the FilterObjects module. By adding the ClassifyObject- and CalculateMath- modules the software calculated the percentage of nuclei positive for Ki67 (link to pipeline in appendix).

3.3 Elevated oxygen treatment

3.3.1 Normobaric and hyperbaric oxygen treatment of organoids

Organoids derived from lung tumor patient 1, 2 and 3, were exposed to both control and elevated oxygen treatment.

Thus, three sperate 24-well plates with organoids, passage 1 and 2, were seeded. One control plate with 3 wells of tumor alveolar organoid and 3 wells with tumor bronchiolar organoids. The control was untreated and kept in a humidified incubator at 37°C with 5% CO_2 and 5% O_2 (Panasonic, MCO-170MUV-PE). The second plate was treated with 100% O_2 for 90 minutes every day for consecutive 5 days at normal atmospheric pressure (1 bar). The last plate was treated in 100% O_2 at elevated ambient pressure (2.4 bar, 14 msw (meters of sea water)) at the same interval as the 1 bar plate. An OXYCOM 250 ARC (Hypcom) oxygen chamber was used to conduct both the normobaric and hyperbaric treatment. The pressure was carefully increased and decreased over a time interval of 10 minutes between 1 bar and 2.4 bar before and after the 90-minute interval, to not risk any unnecessary harm to the organoids by the increasing pressure. Every 30 minute of the hyperbaric treatment, a O_2 flush was conducted to keep the O_2 level at 100% throughout. Both the normobaric oxygen treatment and the hyperbaric oxygen was conducted in the oxygen chamber with the temperature of an average of 37°C. In-between the hyperoxic treatments, these organoids were kept in the same condition as the control plate.

IF staining was performed for investigation of treatment effects. The staining with the proliferation marker Ki67 was performed two times for each treatment group. Representative areas of expression for the control groups were chosen, however, for the treatment groups all present organoids on sections were used for quantification.

3.3.2 Temperature calibration of oxygen chamber

The temperature inside the OXYCOM 250 ARC chamber during the treatment sessions was achieved by heating the chamber with a heat gun before the treatment, in addition to a hot water bag kept inside the chamber throughout the experiment. The temperature of the chamber was monitored by a thermometer. The temperature was held between 39°C and 35°C. This procedure was elucidated through pilot studies.

3.4 Imaging Mass Cytometry

3.4.1 Immunostaining for Hyperion (FFPE staining workflow)

Formalin fixed paraffin embedded control samples or organoid tissue specimens on Superfrost plus microscope slides (Thermo Fisher Scientific,10149870) were labeled with pencil before deparaffinization in xylene (2x10 minutes), decreasing levels of ethanol (100% x2, 96% x2, 70% x1 and 50% x1) and finally rehydration in H_2O, for 5 minutes each. Heat induced target retrieval was achieved in a decloaking chamber. The decloaking chamber was runed at 95°C for 30 minutes. The heat-induced epitope retrieval was conducted in DAKO Target Retrieval Solution (Dako, s1699). At the end of the program, the decloaking chamber was cooled down to 80°C followed by a 20-minute incubation at room temperature to allow the slides to cool down. Further, the slides were washed 10 minutes in milliQ water, followed by a 10-minute wash with PBS (Sigma, P1379) with 0.1% Tween-20 (Sigma, D8537). Both washing steps were executed with careful shaking to achieve reduction of unspecific binding. The tissue on the slides were encircled with hydrophobic pen (DAKO, S2002). Blocking buffer (PBS w/5% BSA and 0.1% Tween-20) was added to the tissue for incubation for 45 minutes at room temperature in a hydration chamber. Immediately after the blocking step, the primary antibody mix (Table 4 and 5) was added, followed by incubation at 4°C, overnight. Primary antibody solution contains antibodies diluted in 0.5% BSA in PBS. The primary antibody mix was centrifuged for 5 minutes at 1000G in 4°C. The following day, the slides were washed for 2x8 minutes in PBS w/0.1% Tween-20 followed by 2x8 minute wash in PBS. Both of these washing steps were performed with gentle agitation. Subsequently, the tissue was stained with 250 µM Intercalator-Ir (Fluidigm, 201192B) in PBS for 30 minutes in

room temperature, followed by one wash with PBS and one with milliQ water, each for 5 minutes. The slides were dried without direct contact between tissue paper and sample. The fully stained slides were stored in a at 4°C inside a container to avoid dust. In this protocol, all solutions were made by using MilliQ water and kept in plastic bottles to avoid contaminations of heavy metals.

Table 4: Organoid Panel

Element	Mass	Target	Clone	Vendor	Cat#	Dilution
Pr	141	K5/6	D5/16B4	Millipore	MAB1620	1:25
Nd	142	EGFR	D38B1	Fluidigm	3142013D	1:100
Nd	143	Vimentin	D21H3	Fluidigm	3143027D	1:100
Nd	144	p-Tyr	p-Tyr-100	Fluidigm	3144024D	1:50
Nd	145	Laminin	poly	Thermo Fisher	PA1-6730	1:800
Nd	146	TNF-alfa	MAb11	Fluidigm	3146010B	1:50
Nd	148	pan-keratin	C11	Fluidigm	3148022D	1:100
Sm	149	STFPC	poly	Thermo Fisher	PA5-76631	1:25
Eu	151	TRP63	poly	Abcam	ab53039	1:50
Eu	153	AXL	A431	R&D Systems	AF154	1:500
Sm	154	HIF1a	EP1176Y	Abcam	ab185238	1:25
Gd	158	E-cadherin	2,40E+11	Fluidigm	3158029D	1:50
Gd	160	VEGFA	EP1215Y	Abcam	ab210073	1:25
Dy	162	LGR5	poly	Abcam	ab75732	1:50
Dy	163	TGFbeta	TW4-6H10	Fluidigm	3163010B	1:50
Dy	164	CK7	RCK105	Fluidigm	3164028D	1:100
Ho	165	b-catenin	D13A1	Fluidigm	3165032D	1:200
Er	166	AXL	7e10	Thermo Fisher	MA5-15504	1:250
Er	168	ki67	B56	Fluidigm	3168022D	1:250
Tm	169	Collagen type I	poly	Fluidigm	3169023D	1:50
Yb	171	Histone H3	D1H2	Fluidigm	3171022D	1:1000
Yb	172	Cleaved Caspase3	5A1E	Fluidigm	3172027D	1:25
Yb	174	K8/18	C51	Fluidigm	3174014A	1:50
Lu	175	pan-actin	D18C11	Fluidigm	3175032D	1:50

Table 5: Organoid Immune Cell Panel

Element	Mass	Target	Clone	Vendor	Cat#	Dilution
Pr	141	K5/6	D5/16B4	Millipore	MAB1620	1:25
Nd	142	EGFR	D38B1	Fluidigm	3142013D	1:100
Nd	143	Vimentin	D21H3	Fluidigm	3143027D	1:100
Nd	144	p-Tyr	p-Tyr-100	Fluidigm	3144024D	1:50
Nd	145	Laminin	poly	Thermo Fisher	PA1-6730	1:800
Nd	146	TNF-alfa	MAb11	Fluidigm	3146010B	1:50
Nd	148	pan-keratin	C11	Fluidigm	3148022D	1:100
Sm	149	STFPC	poly	Thermo Fisher	PA5-76631	1:25
Nd	150	PD-L1	E1L3N	Fluidigm	3150031D	1:25
Eu	151	TRP63	poly	Abcam	ab53039	1:50
Eu	153	AXL	A431	R&D Systems	AF154	1:500
Sm	154	HIF1a	EP1176Y	Abcam	ab185238	1:25
Gd	155	FoxP3	236A/E7	Fluidigm	3155016D	1:25
Gd	156	CD4	EPR6855	Fluidigm	3156033D	1:100
Gd	158	E-cadherin	24e10	Fluidigm	3158029D	1:50
Tb	159	CD68	KP1	Fluidigm	3159035D	1:50
Gd	160	VEGFA	EP1215Y	Abcam	ab210073	1:25
Dy	161	CD20	H1	Fluidigm	3161029D	1:50
Dy	162	CD8a	C8/144B	Fluidigm	3162036D	1:50
Dy	163	TGFbeta	TW4-6H10	Fluidigm	3163010B	1:50
Dy	164	CK7	RCK105	Fluidigm	3164028D	1:100
Ho	165	PD-1	EPR4877(2)	Fluidigm	3165039D	1:25
Er	166	AXL	7e10	Thermo Fisher	MA5-15504	1:250
Er	167	Granzyme B	EPR20129-217	Fluidigm	3167021D	1:200
Er	168	ki67	B56	Fluidigm	3168022D	1:250
Tm	169	Collagen type I	poly	Fluidigm	3169023D	1:50
Er	170	CD3	poly	Fluidigm	3170022D	1:50
Yb	171	Histone H3	D1H2	Fluidigm	3171022D	1:1000
Yb	172	Cleaved Caspase3	5A1E	Fluidigm	3172027D	1:25
Yb	173	CD45RO	UCHL1	Fluidigm	3173016D	1:50
Yb	174	K8/18	C51	Fluidigm	3174014A	1:50
Lu	175	pan-actin	D18C11	Fluidigm	3175032D	1:50

3.4.2 MaxPar Antibody Labeling

Some of the antibodies for Hyperion was conjugated in-house using the Maxpar X8 Antibody Labeling Kit (201300, Fluidigm). The protocol included in the kit was used. The kit contains polymers, loading buffer (L-buffer), reduction buffer (R-buffer), conjugation buffer (C-buffer), and wash buffer (W-buffer). If not otherwise mentioned, all of the centrifugation steps were performed at 12,000 RCF at RT and spin columns was discarded at each of the necessary steps. MaxPar X8 polymer was thawed to RT and dissolved in 95 µL of L-buffer with 5 µL of the specific lanthanide (heavy metal) ion solution followed by 40 min incubation at 37°C in water bath. Concentration of antibodies to be conjugated was measured on a Nanodrop 2000 spectrophotometer (Thermo Scientific). Calculation of antibody equivalent to 100 µg was added to a 50 kDa filter (MilliporeSigma, UFC505008, Saint-Louis, MO, USA) before the total volume was adjusted to 400 µL with R-buffer and spun down for 10 minutes. The antibody was reduced by adding 100 µL of 4 mM TCEP (MilliporeSigma, 646547) in R-buffer and incubated for 30 minutes at 37°C. The antibody was then washed by addition of 300 µL C-buffer, spun down for 10 minutes, washed again with 400 µL C-buffer and spun down for 10 minutes. The metal-loaded polymer was transferred to a 3 kDa filter (MilliporeSigma, UFC500308) along with 200 µL L-buffer and spun down for 25 minutes, followed by an additional wash by 400 µL of C-buffer, then spun down for 30 minutes. Antibody reduction was quenched by adding 300 µL of C-buffer and spun down for 10 minutes, followed by a washing step by addition 400 µL C-buffer and spun down for 10 minutes. The metal loaded polymer was resuspended in 80 µL C-buffer and transferred to the 50 kDa filter with the reduced antibody and incubated at 37°C in water bath for 90 minutes to conjugate the antibody. The conjugation was followed by a washing step with the addition of 200 µL W-buffer and spun down for 10 minutes, continued by 3 additional washing steps with 400 µL of W-buffer and spun down for 10 minutes each. The conjugated and purified antibody was resuspended in 10 µL of W-buffer and measured by the Nanodrop in order to calculate the volume of antibody stabilizer (CANDOR, Bioscience) needed to elute the antibody at a concentration of 500 µL/mL. After removing the W-buffer by spinning down for 10 minutes the calculated volume for antibody stabilizer was added to the filter before inversion of the filter in a new collection tube. The antibody was collected by centrifugation for 2 minutes at 1000 RCF. The conjugated antibody was stored at 4°C until use.

3.4.3 Hyperion setup and operation

The initially setup of the Hyperion (Hyperion Imaging System, Fluidigm) was performed by the Flow Cytometry Core Facility at UiB. A smartphone was used to image the sample slide. The image was uploaded into the HTI module in the Hyperion System, where the slide was loaded into the sample stage. Panoramas were made based on the tissue location on the image scan and potentially xy offsets from image to the actual sample was taken into account at this stage. Calibration of the laser intensity was performed by laser ablating non-relevant areas of the sample with different intensities. Optimal laser intensity was chosen such that the sample was ablated, but the SuperFrost+ was not burned. Following the calibration of the intensity, ROIs were selected from the panorama image. Acquisition template including all metals in used panel with corresponding markers was selected to all the ROIs. In addition, the desired laser intensity and ablation frequency (200Hz, standard frequency) was assigned to the ROIs. Finally, the sample ROIs were ablated, and multiplexed images were created and exported as a .mcd file. The .mcd files are datafiles which contains all valuable data from the IMC-experiment.

3.4.4 Hyperion data analysis pipeline

Exported .mcd file was opened in MCD Viewer software (Fluidigm, v7.0), or histoCAT++ (Bodenmiller Lab) was used as a substitute software for Mac users, where the staining quality was evaluated for each of the markers used in the stain protocol, in all the different ROIs and tissue types. Quality evaluation was performed subjectively based on the signal intensity (auto threshold max), from spillover from neighbor channels and expected staining patterns. Based on the evaluation, images of the working markers were exported as .omne.tiff images for further analysis. For segmentation, the folder of exported images was subsequently uploaded into CellProfiler software (Broad Institute Inc., v.4.0.4) (link to pipeline in appendix)**.** Image masks were made based on the intensity of the two Iridium DNA intercalator isotopes, in addition to the Histone H3 antibody stain. The two Iridium isotopes were scaled for visibility into a “DNA” image. Nuclei were identified using the IdentifyPrimaryObjects module, “DNA” image was used as input. The cells were then identified by using IdentifySecondaryObjects module with a 1-pixel expansion rate from the nucleus, by using the IdentifyPrimaryObjects as input object.

The cytoplasm was identified by using the IdentifyTertiaryObjects module using both IdentifyPrimaryObjects and IdentifySecondaryObjects as input objects, where cytoplasm equals the larger object (IdentifySecondaryObjects) subtracted by the smaller object (IdentifyPrimaryObjects). The nuclei, cell and cytoplasm objects were converted into the final image masks (unit16 color format). Cell masks were saved in the same folder as the original .omne.tiff files exported from MCD viewer. Each ROI of the respectively experiments were exported into histoCAT (Bodenmiller Lab, v1.76) in their original folders. First, phenograph clustering was performed. The clusters were made by selecting samples of interest, as well as markers of interest. We used CK7, K8/18, E-cadherin, vimentin, TRP63, betaCatenin and panActin for the clustering. A heatmap was generated to visualize the relative expression of the markers of interest in the different phenograph clusters. We further applied the t-distributed stochastic neighbor embedding (t-SNE) algorithm using the same markers as selected for the phonograph clustering. For visualization of the tSNE, the samples of interest were selected, and the two tSNE axes were selected in the channel's menu, phenograph option were selected in the heatmap menu, and scatter was chosen for analyzation.

4. Results

4.1 Development of a human airway organoid model

The protocol by Sachs *et al.* (39) was used as a base of the establishment of the patient derived organoid protocol in this thesis. The protocol gave a 100% success rate of establishment of organoids (Figure 4.1). From all these resection specimens, the establishment of NSCLC derived organoids were successful. Furthermore, establishment of organoids following cryopreservation was also successful.

Both establishment of tumor organoids cultured in alveolar- and bronchiolar differentiation medium was successful. L1, L2 and L3 were cultured in both differentiation mediums, while L4, L5 and L6 were cultured only in bronchiolar differentiation medium. Typically, better growth of organoids was observed in the bronchiolar differentiation medium organoids compared to the alveolar differentiation medium (data not shown).

The patient derived organoids were successfully cultured for up to 7 passages, or around 14 weeks in total (data not shown).

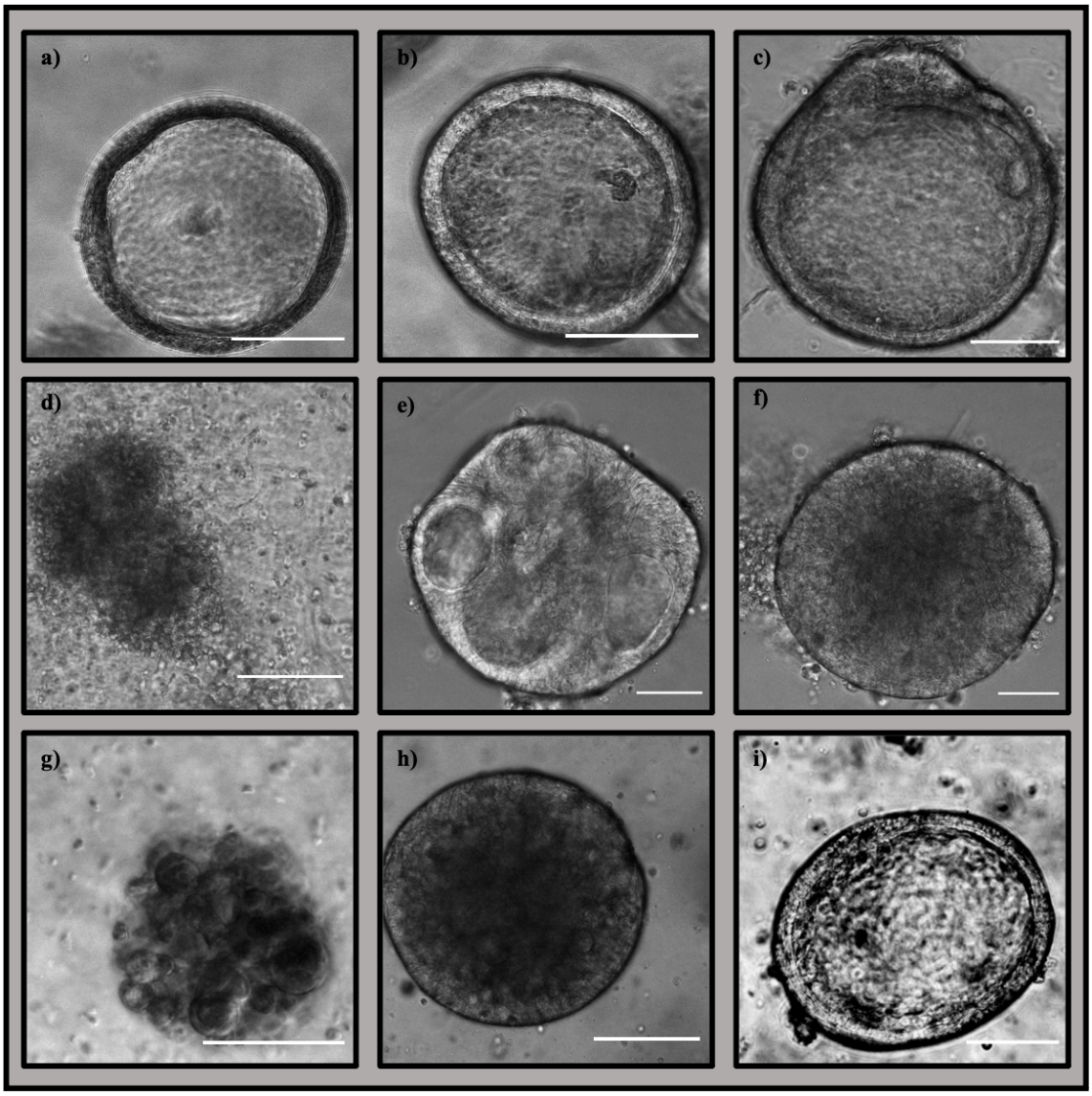

Figure 4.1: Established patient derived organoids. Successfully established patient derived organoids in culture. a) Alveolar differentiated organoid derived from L1. b) Bronchiolar differentiated organoid derived from L1. c) Alveolar differentiated organoid derived from L2. d) Bronchiolar differentiated organoid derived from L2. e) Alveolar differentiated organoid derived from L3. f) Bronchiolar differentiated organoid derived from L3. g) Bronchiolar differentiated organoid derived from L4. h) Bronchiolar differentiated organoid derived from L5. i) Bronchiolar differentiated organoid derived from L6. Scalebar 100 µm.

4.2 Characterization of organoids compared to tumor of origin.

Characterization of organoids compared to NSCLC tumors they derive from were performed under supervision of pathologist Dr. Maria Ramnefjell, at Department of Pathology, Haukeland University Hospital. In addition, Next-generation sequencing (NGS) data from the adenocarcinomas were received. The histological comparison was mainly performed by comparing Hematoxylin and Eosin (HE) stained sections and Alcian blue – Periodic Acid Schiff (AB-PAS) histochemistry stained sections of both organoids and lung tumor tissue of the patient they derived from. Additionally, characterization of the different organoid cultures was performed by immunofluorescence (IF) staining with the proliferation marker Ki67 and ultimately with a panel of isotope labelled antibodies by imaging mass cytometry (IMC).

4.2.1 Characterization of patient lung tumor 1 and patient derived organoids

The first patient lung tumor (L1) specimens received was an adenocarcinoma. Initially HE stains of patient tumor and patient derived organoids were used for comparison and characterization (Figure 4.2). L1 is characterized as a well differentiated adenocarcinoma displaying acinar growth patterns. The tumor tissue is hard to separate from the benign lung tissue. The most prominent feature of patient specimen is desmoplastic stroma. The NGS of the patient tumor was negative for the tested gene mutations (PIK3CA, BRAF, EGFR, NRAS and KRAS). The patient derived organoids display similar characteristics to the patient tumor tissue they derive from.

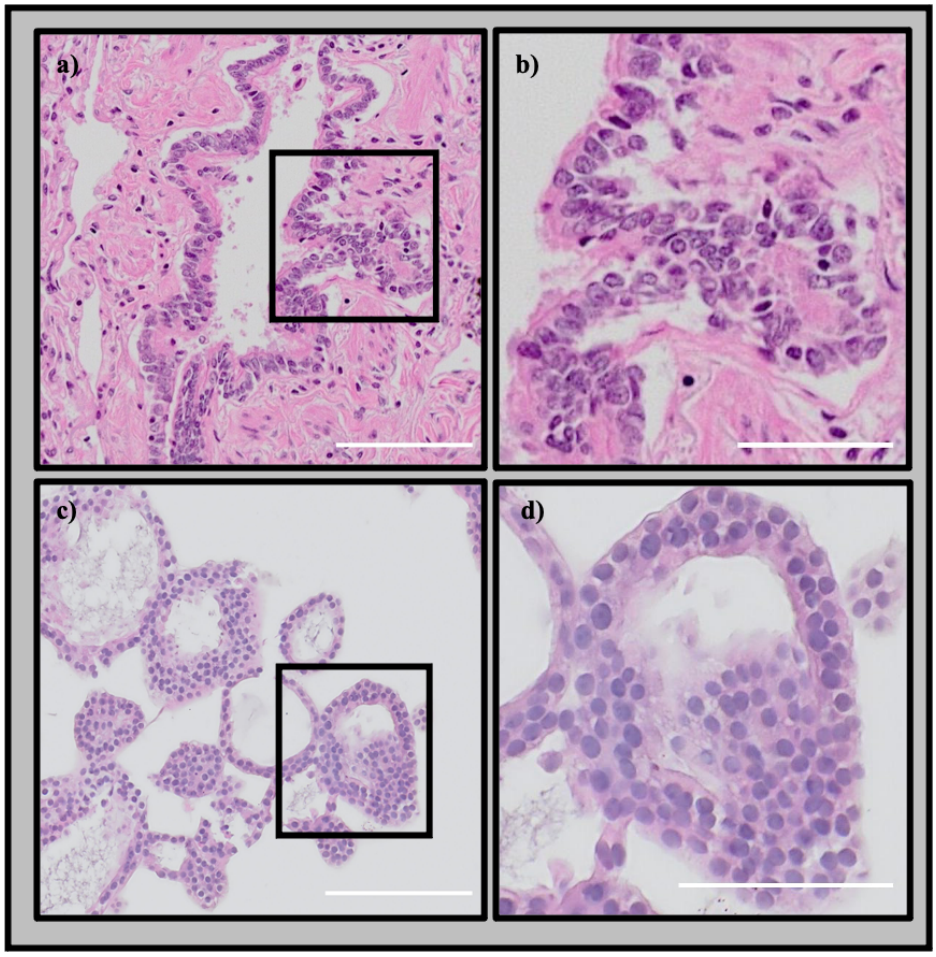

Figure 4.2: Hematoxylin and eosin (HE) stain of patient lung tumor 1 and patient derived organoids. a) HE-stain of patient lung tumor 1. b) HE-stain of patient lung tumor 1, zoomed insert. c) HE-stain of derived organoids from patient lung tumor 1. d) HE-stain of derived organoids from patient lung tumor 1, zoomed insert. Scalebar 100 µm (a and c). Scalebar 50 µm (b and d)

Patient derived organoids derived from L1 display mainly circular/oval structural growth patterns. Most of the organoids have a hollow central lumen with layers of cells lining the outer edges of the organoid structures as seen in Figure 4.2C and D. The organoids were mostly around 100-200 µm in diameter. Furthermore, the AB-PAS histochemistry which detects mucin revealed that the organoids produce mucin and that the hollow core is mostly positive for mucin (Figure 4.3).

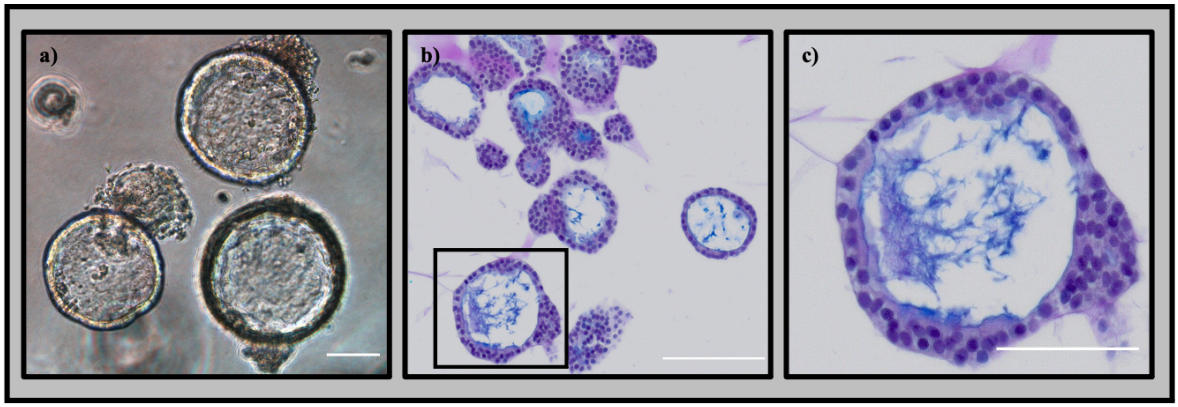

Figure 4.3: Patient derived lung tumor organoids in culture and with the mucin stain AB-PAS. a) Derived organoids from lung tumor patient 1 in culture. b) AB-PAS stain of derived organoids from lung tumor patient 1. c) AB-PAS stain of derived organoids from lung tumor patient 1, zoomed insert. a) and b) scalebar 100 µm, c) scalebar 50 µm.

4.2.2 Characterization of patient lung tumor 2 and patient derived organoids

The second patient lung tumor (L2) received was a lepidic adenocarcinoma. Initially HE- stain of both lung tumor and patient derived organoids was used for comparison and characterization (Figure 4.4). L2 is a lepidic predominant adenocarcinoma, the most prominent feature of patient tumor is Pneumocytic-type malignant cells. The malignant cells grow only along normal lung structures such as alveoli, as seen in Figure 4.4. Low cell division rates are typically observed in the lepidic adenocarcinomas. The malignant cells are hard to detect. The NGS results for the patient tumor were negative for all tested mutations. Thus, the organoids were difficult to culture over a long period of time, and they grew slower for each passage. Subsequently, the derived organoids display largely similar characteristics compared to the tumor.

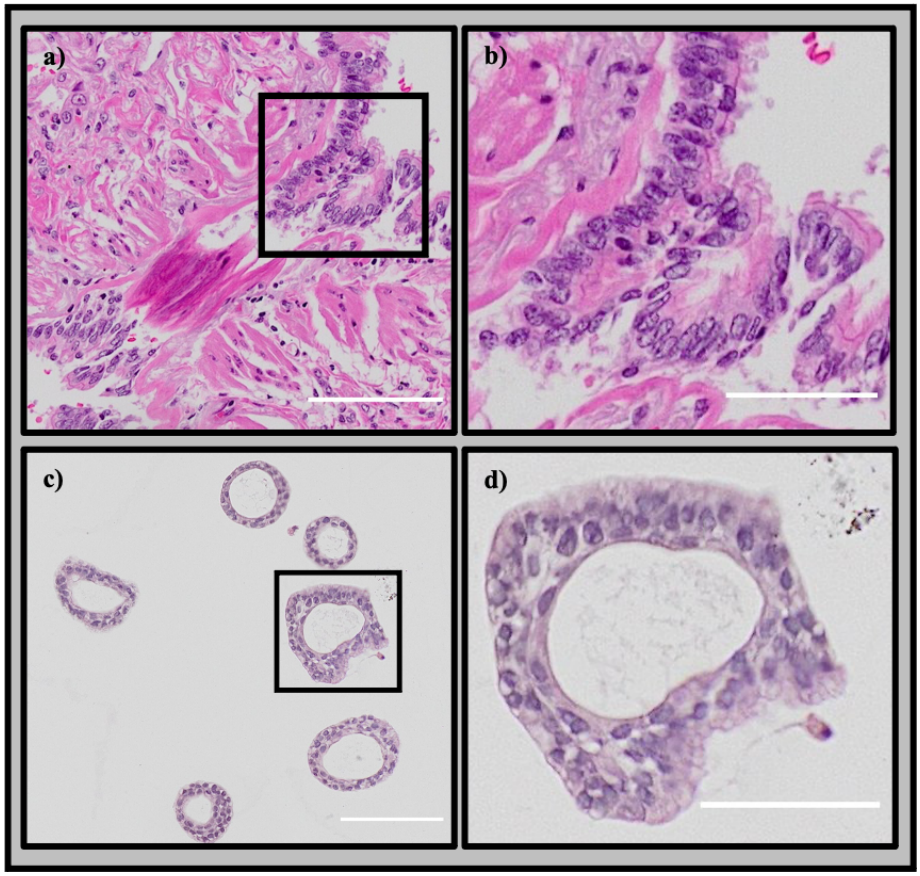

Figure 4.4: Hematoxylin and eosin (HE) stain of patient lung tumor 2 and patient derived organoids. a) HE-stain of patient lung tumor 2. b) HE-stain of patient lung tumor 2, zoomed insert. c) HE-stain of derived organoids from patient lung tumor 2. d) HE-stain of derived organoids from patient lung tumor 2, zoomed insert. Scalebar 100 µm (a and c). Scalebar 50 µm (b and d)

Patient derived organoids from L2 grew in a variation between compact organoids and hollow organoids, and some of the organoids had smaller vacuoles as seen in Figure 4.5. The bronchiolar differentiated organoids died after the first passage. The organoids were typically 50-150 µm in diameter. Subsequently, the AB-PAS stain shows that the organoids have moderate mucin production.

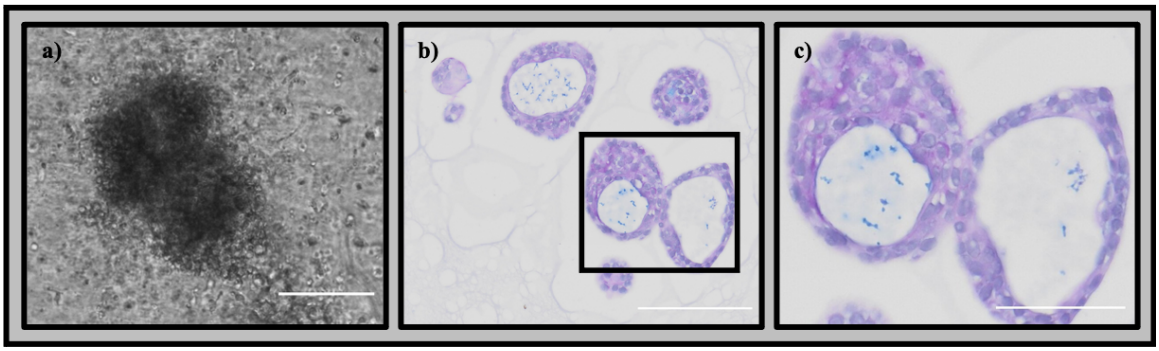

Figure 4.5: Patient derived lung tumor organoids in culture and with the mucin stain AB-PAS. a) Derived organoids from lung tumor patient 2 in culture. b) AB-PAS stain of derived organoids from lung tumor patient 2. c) AB-PAS stain of derived organoids from lung tumor patient 2, zoomed insert. a) and b) scalebar 100 µm, c) scalebar 50 µm.

4.2.3 Characterization of patient lung tumor 3 and patient derived organoids

The third patient lung tumor (L3) received was an adenocarcinoma. The initial HE-stain of patient tumor and the derived organoids used for comparison and characterization shows that patient tumor is mostly recognized by an acinar growth pattern. Further, the NGS results of the patient tumor are positive for EGFR deletion in chromosome 19. This can be detected in organoids by EGFR del19 immunofluorescent staining (IF). HE-stain of patient tumors compared to the derived organoids shows similar characteristics and growth patterns, with large nuclei, as seen in Figure 4.6.

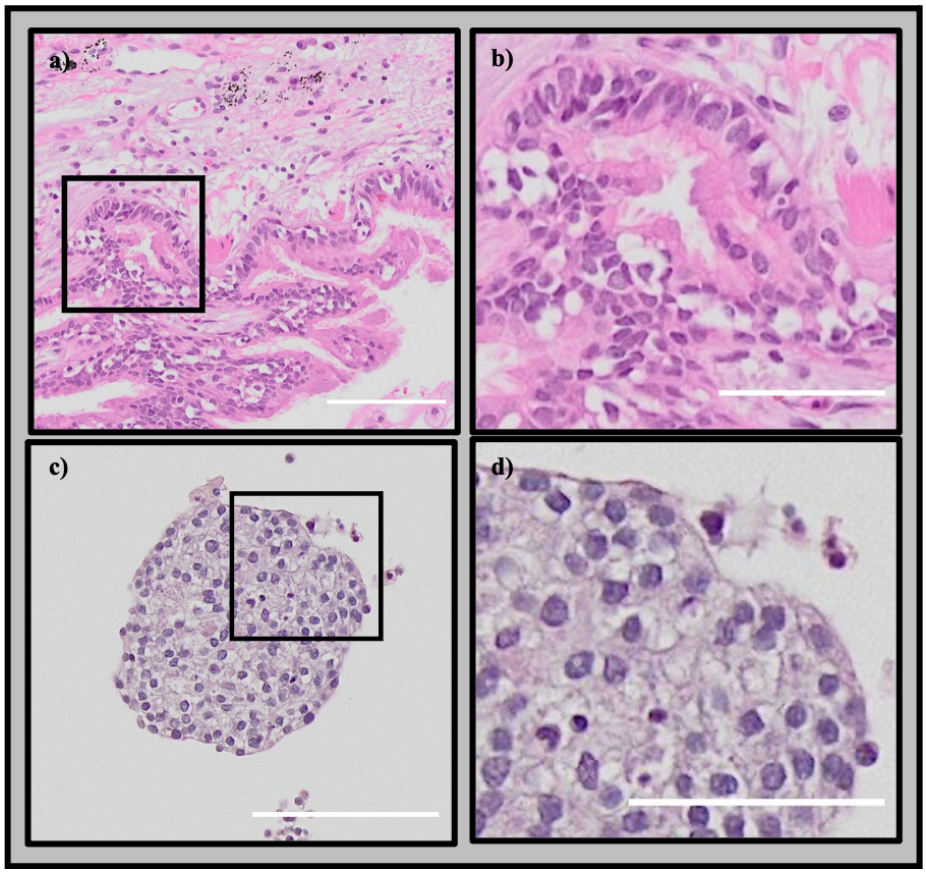

Figure 4.6: Hematoxylin and eosin (HE) stain of patient lung tumor 3 and patient derived organoids. a) HE-stain of patient lung tumor 3. b) HE-stain of patient lung tumor 3, zoomed insert. c) HE-stain of derived organoids from patient lung tumor 3. d) HE-stain of derived organoids from patient lung tumor 3, zoomed insert. Scalebar 100 µm (a and c). Scalebar 50 µm (b and d)

Patient derived tumor organoids from L3 have a large range of different growth patterns. From compact structures, to organoids containing one or several small vacuoles, or organoids containing large vacuoles. This is shown in Figure 4.7. Both alveolar- and bronchiolar differentiated organoids displayed good growth rates. The organoids from L3 are typically 100-250 µm in diameter, and as seen in Figure 4.7 the more compact organoids are smaller in diameter then the lesser compact organoids. Further, the AB-PAS stain of the organoids shows that these have a rather efficient production of mucin. Finally, IF stain of the L3 derived organoids show that the organoids have the same EGFR mutation as tumor of origin (Figure 4.8).

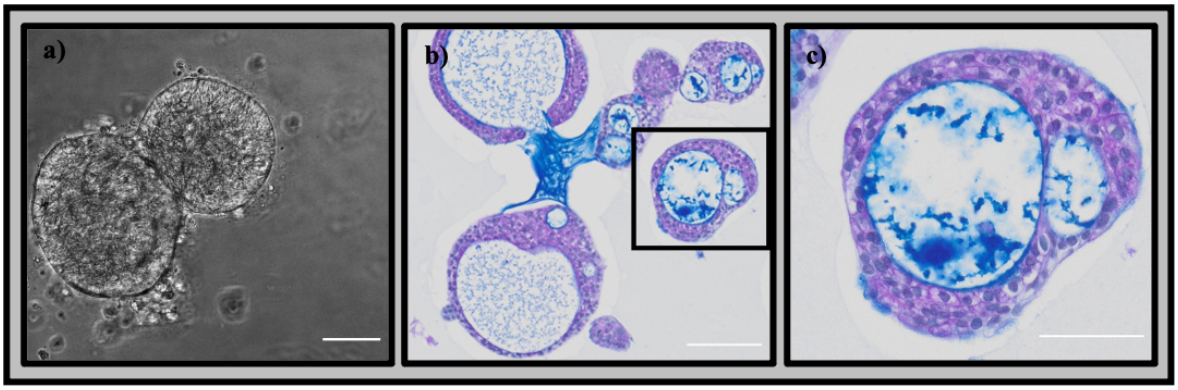

Figure 4.7: Patient derived lung tumor organoids in culture and with the mucin stain AB-PAS. a) Derived organoids from lung tumor patient 3 in culture. b) AB-PAS stain of derived organoids from lung tumor patient 3. c) AB-PAS stain of derived organoids from lung tumor patient 3, zoomed insert. a) and b) scalebar 100 µm, c) scalebar 50 µm.

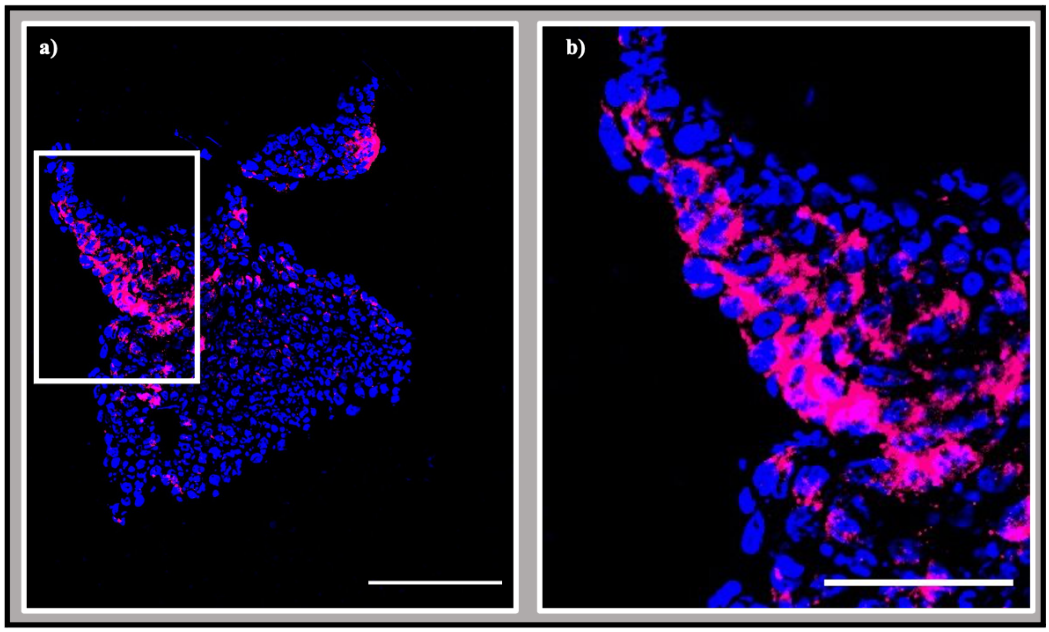

Figure 4.8: EGFR Immunohistochemistry stain of patient derived organoid. IF stain with EGFR antibody on patient derived organoids from L3, DAPI – blue, EGFR - magenta.
a) Overview of organoid with EGFR stain, scalebar 100 µm. b) Organoid with EGFR stain, zoomed insert, scalebar 50 µm.

4.2.4 Characterization of patient lung tumor 4 and patient derived organoids

The fourth patient lung tumor (L4) received is a squamous cell carcinoma. The patient squamous cell carcinoma tumor was large (>7 cm). The initial HE-stain of the patient tumor and the derived organoids performed for comparison and characterization shows that the resection specimen contains no benign lung tissue. HE-stain also shows that the patient tumor is characterized by areas of prominent necrosis, and that the malignant cells are poorly differentiated, which makes it easy to separate malignant and benign cells. Furthermore, the nuclei are irregular in size as well as in chromatin structure, seen in Figure 4.9. Staining with K5/6 antibody of patient tumor performed by the Department of Pathology showed some keratinized tumor tissue in the presence of a few pearl formations. Derived organoids display very similar growth patterns as tumor of origin, with large and irregular nuclei. Thus, there are highly similar characteristics between the organoids and tumor.

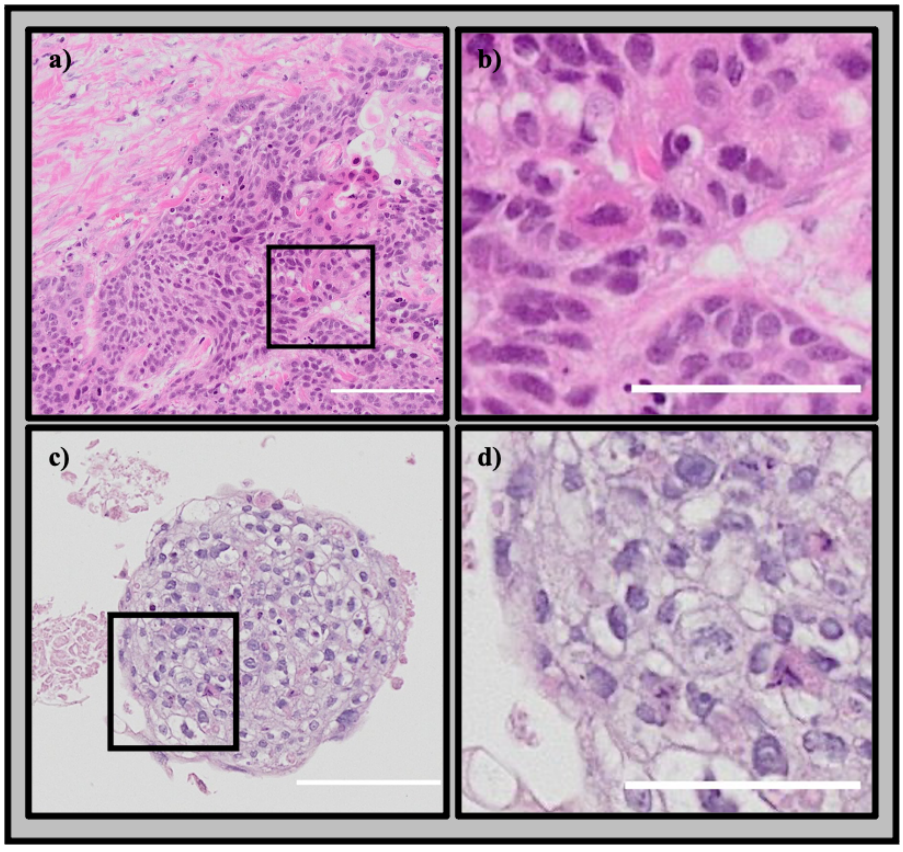

Figure 4.9: Hematoxylin and eosin (HE) stain of patient lung tumor 4 and patient derived organoids. a) HE-stain of patient lung tumor 4. b) HE-stain of patient lung tumor 4, zoomed insert. c) HE-stain of derived organoids from patient lung tumor 4. d) HE-stain of derived organoids from patient lung tumor 4, zoomed insert. Scalebar 100 µm (a and c). Scalebar 50 µm (b and d)

Derived organoids from L4 are only growing in very compact structures with no vacuoles. The organoids are typically 100-200 µm in diameter. The organoids have irregular nuclei, like the tumor of origin. Further the AB-PAS stain of organoids shows little to no production of mucin, seen in Figure 4.10.

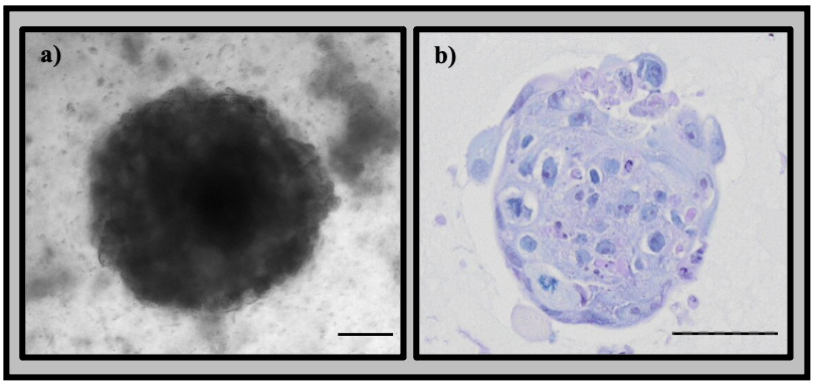

Figure 4.10: Patient derived lung tumor organoids in culture and with the mucin stain AB-PAS. a) Derived organoids from lung tumor patient 4 in culture. b) AB-PAS stain of derived organoids from lung tumor patient 4. a) scalebar 100 µm, b) scalebar 50 µm.

4.2.5 Characterization of patient lung tumor 5 and patient derived organoids

The fifth patient lung tumor (L5) received is an adenocarcinoma. The initial HE-stain performed for comparison and characterization of patient tumor and derived organoids show that the tumor is mostly characterized by an acinar growth pattern with biologically aggressive characteristics, as seen in Figure 4.11. In particular, the tumor consists of areas of macropapillary growth as well as selected areas displaying micropapillary growth pattern, solid isolated groups consisting of a few malignant cells. Some infiltrating single tumor cells observed. The specimen displays a large degree of nuclear pleomorphism, i.e., the nuclei show large variation in size and chromatin structure. Additionally, tumor consists of some areas of prominent necrosis. The NGS results from the patient tumor was negative to all tested mutations. Respectively, some of the organoids have similar characteristics compared to the tumor.

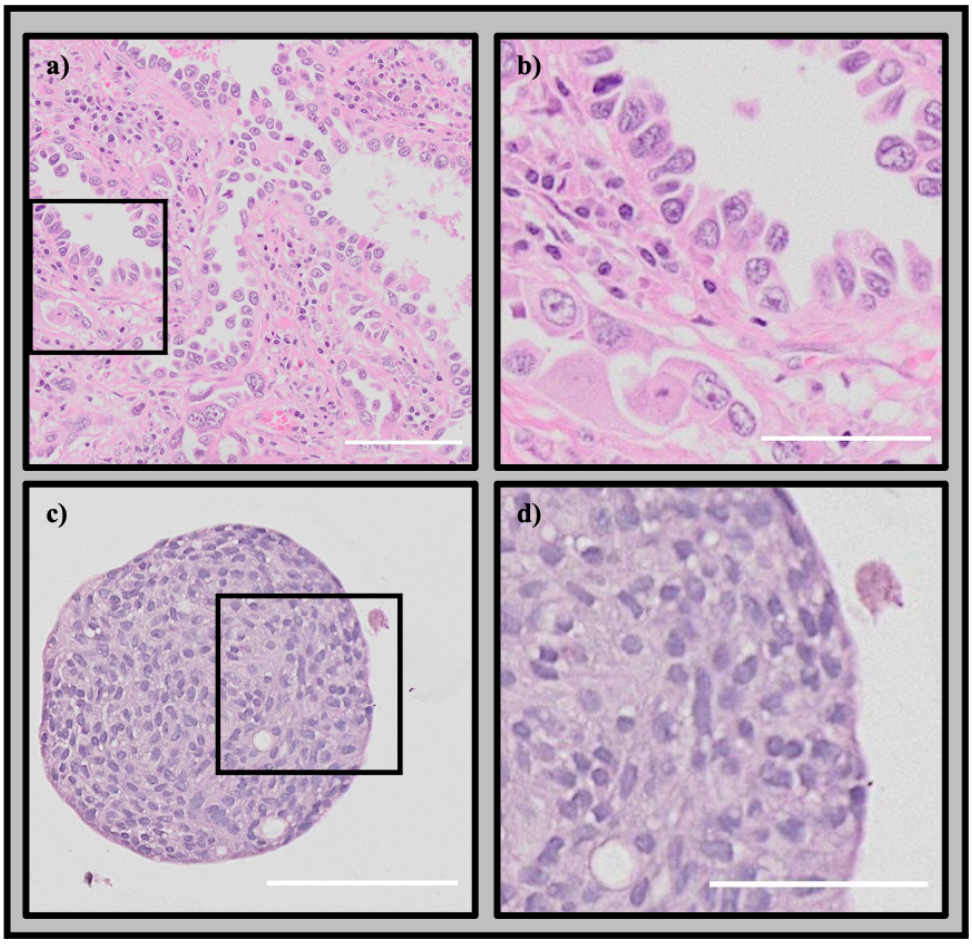

Figure 4.11: Hematoxylin and eosin (HE) stain of patient lung tumor 5 and patient derived organoids. a) HE-stain of patient lung tumor 5. b) HE-stain of patient lung tumor 5, zoomed insert. c) HE-stain of derived organoids from patient lung tumor 5. d) HE-stain of derived organoids from patient lung tumor 5, zoomed insert. Scalebar 100 µm (a and c). Scalebar 50 µm (b and d)

Patient organoids derived from L5 mostly consist of compact structures, some of the organoids have smaller vacuoles, this is seen in Figure 4.11. The organoids are usually 50-150 µm in diameter. AB-PAS stain of the organoids shows some mucin production, seen in Figure 4.12. Some of the organoids seems to resemble the micropapillary growth patterns of the tumor. Ultimately, some of the organoids have similar growth patterns as the tumor of origin. Of note, some of the derived organoids seems to be of normal lung tissue.

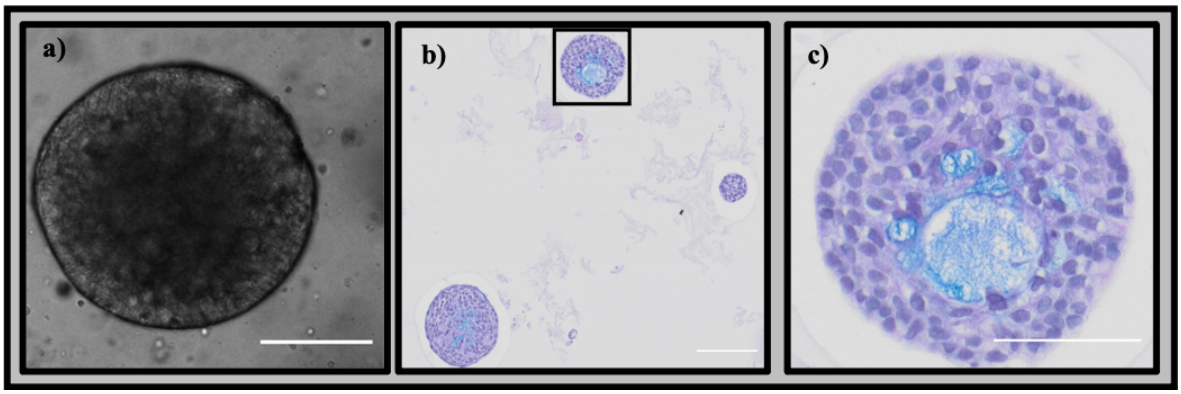

Figure 4.12: Patient derived lung tumor organoids in culture and with the mucin stain AB-PAS. a) Derived organoids from lung tumor patient 5 in culture. b) AB-PAS stain of derived organoids from lung tumor patient 5. c) AB-PAS stain of derived organoids from lung tumor patient 5, zoomed insert. a) and b) scalebar 100 µm, c) scalebar 50 µm.

4.2.6 Characterization of patient lung tumor 6 and patient derived organoids

The sixth and final patient lung tumor (L6) received is the second squamous cell carcinoma in the sample set. Initial HE-stain of patient tumor and derived organoids were performed for comparison and characterization (Figure 4.13). The tumor L6 is quite undifferentiated, but still more differentiated then the first squamous cell carcinoma tumor received (L4). The tumor consists of small necrotic foci and larger areas prominent of palisading necrosis (Figure 4.13 a). The tumor has a growth pattern characteristic of LUSC with tumor cells in large clusters/sheets. Further, a high degree of nuclear pleomorphism is observed; the nuclei are irregular in size as well as in chromatin structure with prominent nuclei (these features are not sufficient to distinguish squamous cell carcinoma from adenocarcinoma). Cells are rich in light eosinophilic cytoplasm. Apoptosis and mitosis are observed, in addition to intercellular bridges, which only exists in squamous cell carcinomas. The malignant cells grow in palisade formation, resembling a basal formation (Figure 4.14). Finally, single cell keratinization is observed. Subsequently, the organoids are largely similar in characteristics compared to the tumor.

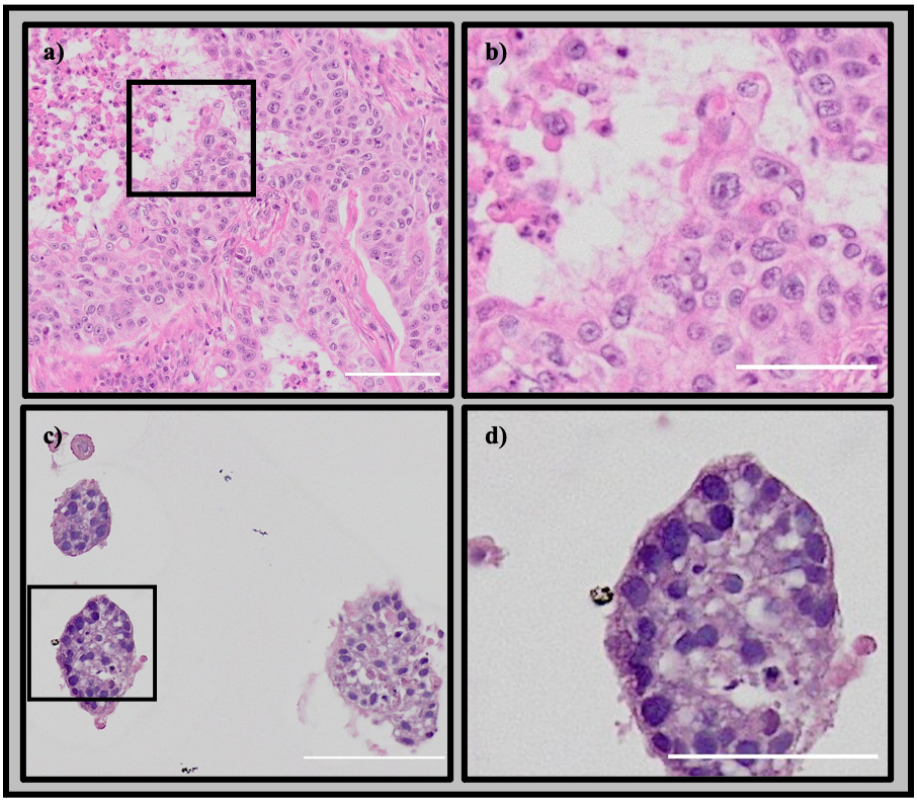

Figure 4.13: Hematoxylin and eosin (HE) stain of patient lung tumor 6 and patient derived organoids. a) HE-stain of patient lung tumor 1. b) HE-stain of patient lung tumor 6, zoomed insert. c) HE-stain of derived organoids from patient lung tumor 6. d) HE-stain of derived organoids from patient lung tumor 6, zoomed insert. Scalebar 100 µm (a and c). Scalebar 50 µm (b and d).

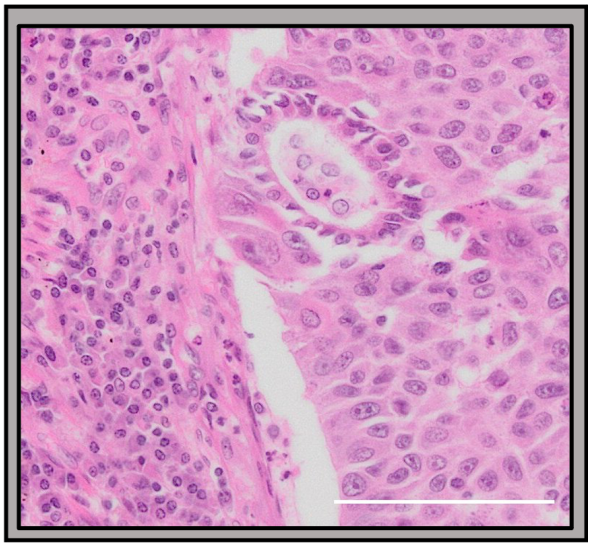

Figure 4.14: Hematoxylin and eosin (HE) stain of patient lung tumor. Figure shows an area of palisade formation in tumor specimen. Scalebar 100 µm.

Derived organoids from L6 tumor display a compact growth pattern, similar to the first squamous cell carcinoma derived organoids (L4). Organoid size varies between 50-200 µm in diameter. Derived organoids from this specimen consist of large and irregularly sized cell nuclei with irregular chromatin, similar to the malignant tissue they derive from. However, cytoplasm borders are unclear, which may be due to suboptimal preparation of the specimen. Further, some organoids seem to display areas with signs of necrosis, and even the palisade formation of the tumor cells in surrounding the necrotic areas, as seen in the malignant tissue they derive from (Figure 4.13 d). Mitotic cells are also observed in the organoid specimens. AB-PAS stain performed on organoids show none to very little production of mucin, as seen in Figure 4.15.

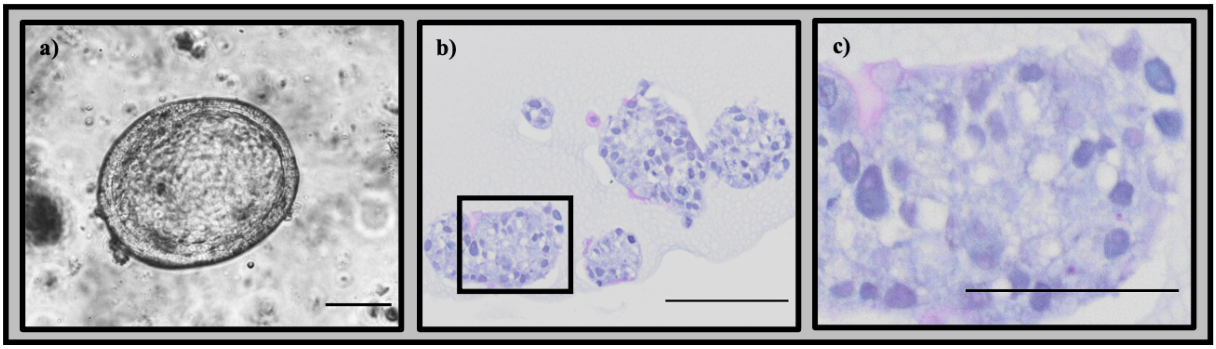

Figure 4.15: Patient derived lung tumor organoids in culture and with the mucin stain AB-PAS. a) Derived organoids from lung tumor patient 6 in culture. b) AB-PAS stain of derived organoids from lung tumor patient 6. c) AB-PAS stain of derived organoids from lung tumor patient 6, zoomed insert. a) and b) scalebar 100 µm, c) scalebar 50 µm.

4.2.7 Ki67 expression in patient derived organoids

For the patient derived organoids with origin from L1-L6, immunofluorescent (IF) staining for the proliferation marker Ki67 was performed to assess proliferation in the organoid cultures. All organoids express Ki67. The staining shows a heterogenous expression pattern of the proliferation marker Ki67 in the different organoids (Figure 4.16).

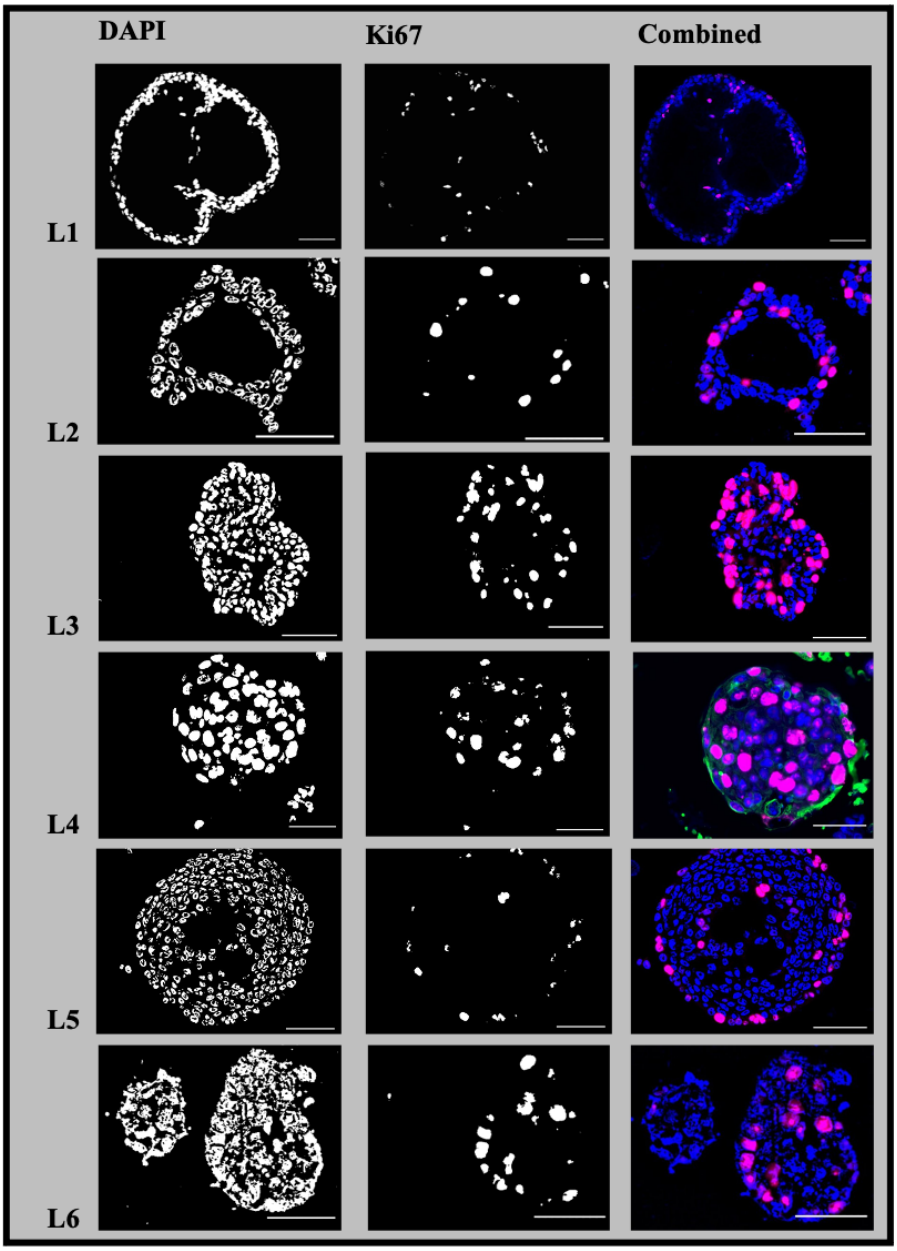

Figure 4.16: Ki67 expression in patient derived lung tumor organoids compared to each other. Expression shown from lung tumor patient 1 to 6 (L1-L6) with DAPI channel, Ki67 channel and combined.

4.3 The effect of normobaric and hyperbaric oxygen treatment on patient derived organoids

Normobaric and hyperbaric oxygen treatment (Norm and HBOT, respectively) were performed on patient derived organoids from L1, L2 and L3. The treatment was conducted over five consecutive days, and 90-minute treatment each day. Organoids were immediately harvested after treatment the last day. IF stain with the proliferation marker Ki67 was performed on the two treatment groups compared to control group as shown in Table 4.2 and Fig 4.17. For all patient organoid cultures, L1, L2 and L3, most derived organoids were successfully harvested from the control group. The least amount of remaining tissue was found in the hyperbaric oxygen treatment group, and in normobaric oxygen treatment group an intermediate amount of tissue remained after treatment.

Table 4.2 Expression of Ki67 in treated organoids compared to controls.

Organoid	Cell - nuclei	Ki67 Pos Nuclei	Percentage Ki67
L1Ctrl	316	33	10,44 %
L1 Norm	227	2	0,88 %
L1 HBO	285	49	17,90 %
L2 Ctrl	312	86	27,56 %
L2 Norm	507	0	0 %
L2 HBO	260	62	23,85 %
L3 Ctrl	537	123	22,91 %
L3 Norm	506	90	17,79 %
L3 HBO	82	7	8,54 %
L3 HBO 2	72	5	6,94 %

The table shows the expression of proliferation marker Ki67 staining detected in organoids derived from organoids treated with normobaric or hyperbaric oxygen therapy (Norm and HBOT, respectively) and control group (Ctrl). The table show the total number of nuclei (as determined by DAPI staining), Ki67 positive nuclei, and calculated percentage of Ki67 expression in the various groups. One representative section was stained and counted for each condition, with the exception of L3 HBO where two sections were analyzed in order to have enough cell to include in the analysis.

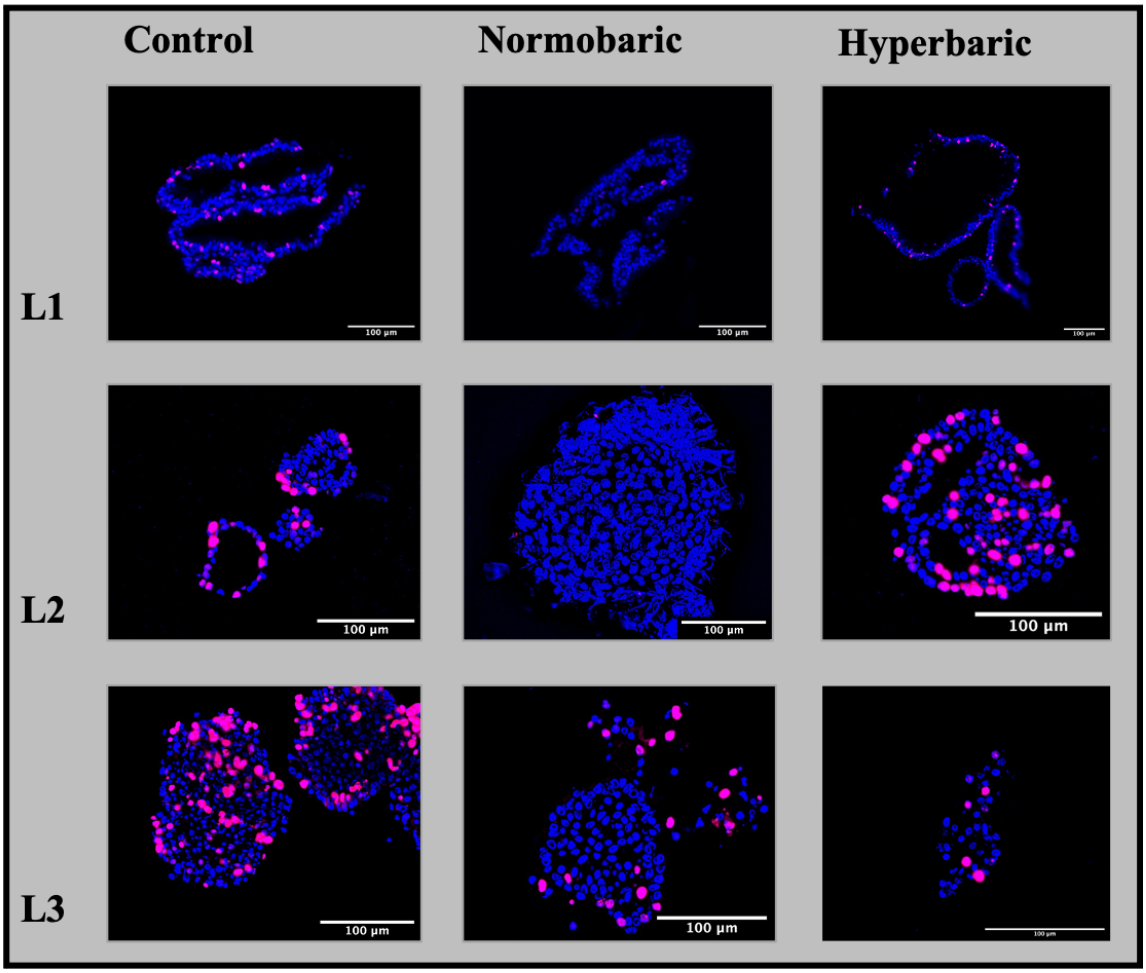

Figure 4.17: Ki67 expression in organoids treated with normobaric- and hyperbaric-oxygen. Three different patient derived organoids treated with normobaric- and hyperbaric oxygen compared to controls. Lung tumor patient 1-3 (L1-L3).

4.4 Imaging Mass Cytometry

The development of an IMC – panel was initiated in order to be able to perform a deeper characterization of the patient derived organoid cultures, as well as deeper investigation of the effect of the elevated oxygen treatment. A selection of IMC exported images is presented here to illustrate the enormous potential of the technique, in addition to deeper characterization of the histoarchitecture, for some of the derived organoids.

4.4.1 Characterization of adenocarcinoma compared to squamous cell carcinoma derived organoids

The L3, adenocarcinoma derived organoids, of both alveolar and bronchiolar differentiation, showed expression of collagen type I, laminin, histone H3, vimentin, E-cadherin, CK7, K8/18, TRP63 as well as Ki67, seen in Figure 4.18 and 4.19.

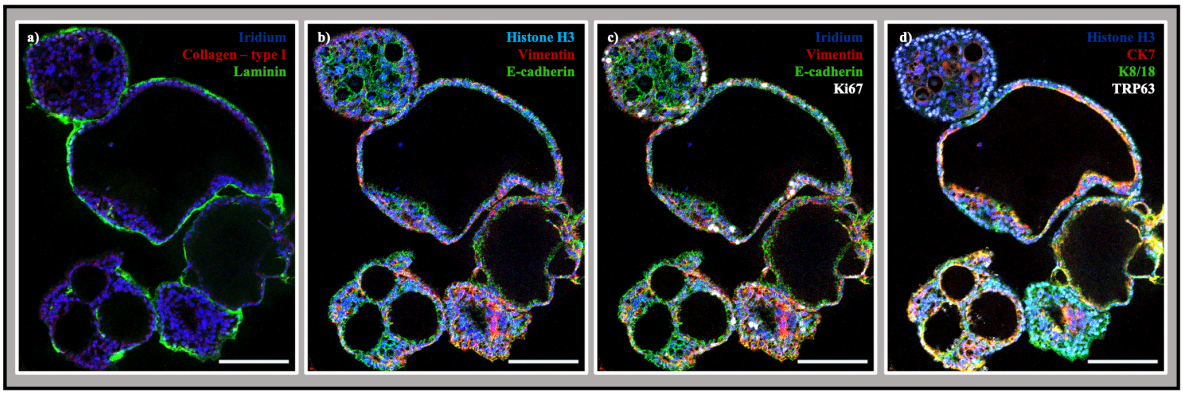

Figure 4.18: L3 P1 Alveolar differentiated patient derived organoids, imaging mass cytometry exported images. a) Iridium – blue, Collagen type I – red, Laminin – Lime. b) Histone H3 – blue, Vimentin – red, E-cadherin – lime. c) Iridium – blue, Vimentin – red, E-cadherin – Lime, Ki67 – white. d) Histone H3 – blue, CK7 – red, K8/18 – lime, TRP63 – white. Scalebar: 100 µm.

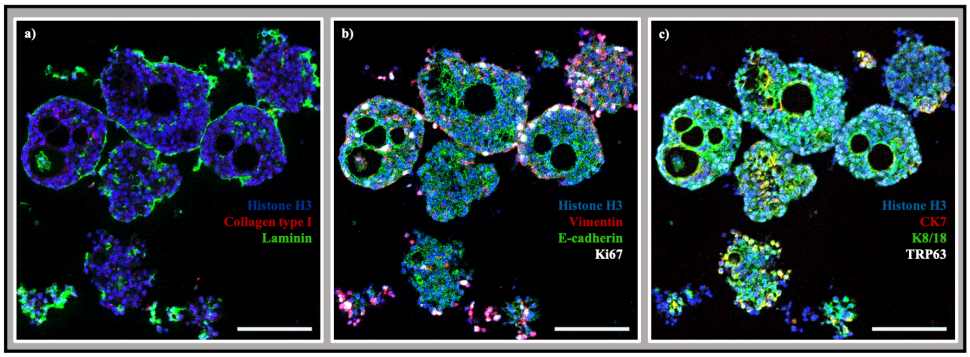

Figure 4.19: L3 P1 Bronchiolar differentiated patient derived organoids, imaging mass cytometry exported images. a) Histone H3 – blue, Collagen type I – red, Laminin – Lime. b) Histone H3 – blue, Vimentin – red, E-cadherin – lime, Ki67 – white. c) Histone H3 – blue, CK7 – red, K8/18 – Lime, TRP63 – white. Scalebar: 100 µm.

The L4, squamous cell carcinoma derived organoids, bronchiolar differentiated, show expression of histone H3, E-cadherin, Ki67, TRP63, and a low expression of K8/18. The organoid structure does not show expression of collagen type I, laminin, vimentin nor CK7. Seen in Figure 4.20.

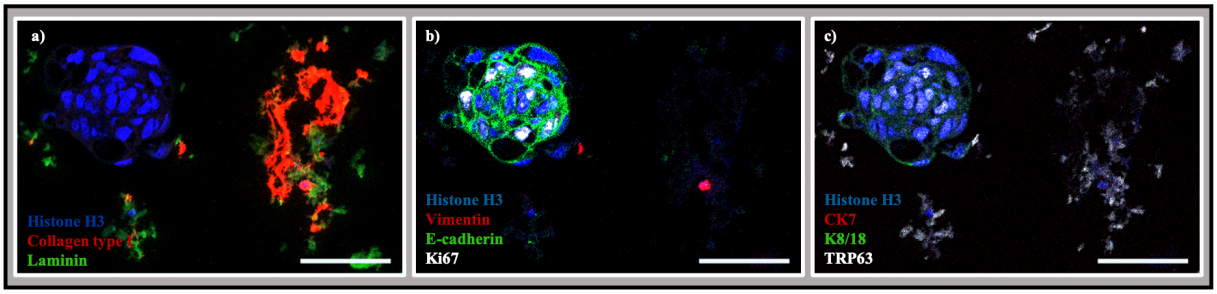

Figure 4.20: L4 P0 Bronchiolar differentiated patient derived organoids, imaging mass cytometry exported images: a) Histone H3 – blue, Collagen type I – red, Laminin – Lime. b) Histone H3 – blue, Vimentin – red, E-cadherin – lime, Ki67 – white. c) Histone H3 – blue, CK7 – red, K8/18 – Lime, TRP63 – white. Scalebar: 100 µm

Phenograph clusters were made from the three samples. Further, a heatmap was generated out of the cluster. In the heatmap, the clusters are represented in rows, and the selected markers in columns. Data are displayed on a scale from zero (blue) to one (yellow). In the tSNE plot, each cluster is highlighted in a different color. Results in Figure 4.20.

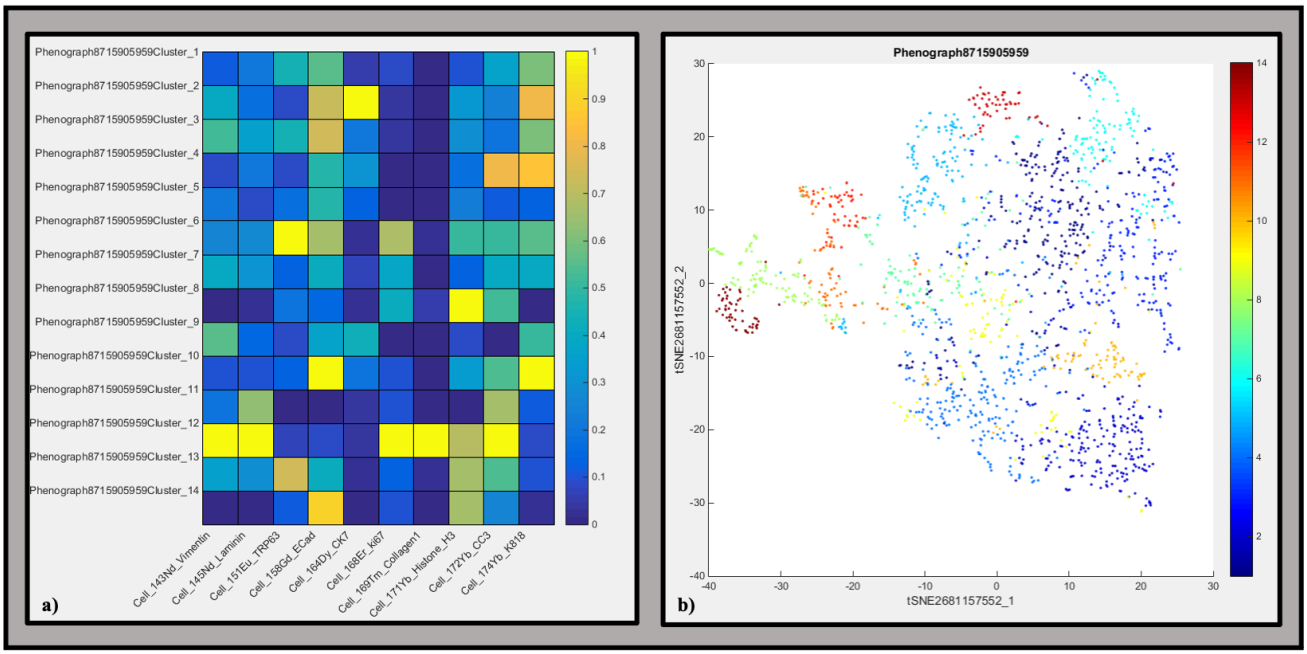

Figure 4.20: Phenograph heatmap and tSNE visualization of clusters from L3 P1, both alveolar and bronchiolar differentiated, and L4 organoids. a) Phenograph heatmap. b) tSNE visualization of phenograph clusters.

5. Discussion

5.1 Methodological considerations

5.1.1 Three-dimensional organoid model

3D patient derived organoids have recently emerged as a unique and robust tool for screening of therapeutic efficiency and toxicity testing. These patient derived *in vitro* organoid models have several advantages compared to the two-dimensional cultures and animal models. First, a patient derived organoid model will give better representation of the tumor heterogeneity than other *in vitro* models as they are derived from different patients and multiple cells as opposed one single cell, that many cell lines used for *in vitro* experiments derive from. Furthermore, they will resemble human biology and tissue functionality better than the *in vivo* animal models, since they maintain the histoarchitecture as well as genetic mutations of the tumor of origin (43). Thus, organoid models represent a particularly good starting point for personalized treatment research. Finally, the method is relatively quick, less expensive, and ethically superior to using animals. However, the patient derived three-dimensional models are not perfect, as they are not vascularized and lack certain cell types *(e.g.,* immune cells*)* that normally appear in the tumor microenvironment *in vivo* (44).

5.1.2 Three-dimensional organoid model in Imaging Mass Cytometry

In order to be able to apply this 3D organoid model for techniques such as IMC and other tissue staining techniques, the harvesting method have been optimized as a part of this master project. We needed to optimize the protocol for embedding the organoids to obtain good results compatible with the downstream histology and IMC analyses. In the start we had problems with the harvesting and was able to only get a few good organoids on each section. To solve this problem centrifuging and heating of equipment in the agar embedding process was added. The optimization gave in general more organoid tissue per section and made it possible to get good and representative staining results. Following our studies, we conclude that the organoid cultures are compatible with the IMC technology.

5.1.3 Elevated oxygen treatment

The temperature in the hyperbaric chamber was reached by heating the chamber in advance of the treatment. An automatic electric heater, calibrated to 37ºC, would of course give a more stable and precise temperature, however electrical apparatus within the oxygen chamber will pose a fire hazard and could therefore not be applied. Thus, there was a slight temperature decrease during the treatment period, although not so much that we believe it would influence the results to any great extent.

The number of organoids harvested in the treatment groups were low, probably due to an hyperoxic inhibition of growth. Thus, usage of IncuCyte platform for quantification to monitor alterations in organoid numbers and size in order to be able to conclude about the treatment effect should be added in the next run of experiments. Furthermore, to be able to harvest enough organoids for downstream analyses, such as a large IMC experiment, the solution could be to have more replicates in the treated groups.

5.1.4 Imaging mass cytometry

Imaging mass cytometry (IMC) is a novel technique. It is the world's first and most proven high-multiplex imaging and single-cell protein analysis (45). IMC allows labeling of tissue sections with up to 40 heavy metal-conjugated antibodies simultaneously (46). The available Hyperion/Helios (Fluidigm platform) Imaging System at UiB, made it possible to apply IMC as a tool for deeper characterization of the patient derived lung tumor organoid model in this project. This technology gave us the opportunity to gather information on the tissue architecture of the derived organoids, as well as the cellular morphology (47). This preliminary work has shown that the IMC technology is also a particularly well suited in combination with organoid models. However, the cost of performing an IMC project is very high, and it is also highly time-consuming technique with respect to panel design and optimalization and downstream analyses.

5.1.4.1 Imaging Mass Cytometry workflow

In an IMC experiment, solid tissue samples, either FFPE or frozen, is sectioned and mounted on glass slides, deparaffinized and rehydrated. We used FFPE sections, which preserves excellent tissue morphology compared to the frozen sections. This can easily be incorporated into routine tissue processing, and storage. The sample sections were subjected to antigen retrieval to expose tissue antigens. These were then blocked with serum proteins to reduce unspecific binding before labeling with a heavy metal conjugated antibody cocktail. Followed by labeling with a heavy metal DNA intercalator (Iridium). After the labeling workflow, Regions of Interest (ROIs) of labeled sections were selected. The IMC-system measures the levels of heavy metal ablated segments of the tissue (1 μm^2) and correspond each of the heavy metal tags to individual pixel intensities in the selected ROIs. Further the analyzed tissue was subjected to cell segmentation by using the DNA intercalator label for identification of nuclei. The cell segmentation is highly dependent on good signal and good titration, and we could observe that the segmentation got better for each test run. For the cell segmentation, we decided to supplement the DNA intercalator Iridium label with the nuclear marker, Histone H3, due to a very good signal. This alteration of the protocol improved the cell segmentation. Finally, the cell masks were analyzed by exporting and importing images to downstream analyzing tools.

The staining procedure for an IMC experiment is rather straight forward once one have gained experience with the complex workflow. However, there are some possible “traps” throughout workflow that we tried to avoid. It is important to use fresh xylene for the dewaxing, in addition, washing steps should be performed by using dedicated containers, never washed in detergent, to avoid barium contamination.

5.1.4.2 Imaging Mass Cytometry panel development

In the development of an IMC panel, a huge number of factors must be taken into consideration. First, we needed to consider which antibodies were relevant for the chosen tissue of interest, namely NSCLC tissues. Furthermore, the choice of the corresponding heavy metal channels for each antibody. We had to consider the in-house antibody inventory. We decided to use the in-house antibody inventory as a foundation for the panel. A growing selection of commercially

available pre-conjugated antibodies are available in selected channels. Some antibodies were purchased, and some central markers were conjugated by us *in-house*. Of note, the success rates vary for the *in-house* conjugation; however, they are great for cost savings and the success rate is expected to increase with experience. Furthermore, some of the available channels are more sensitive, so markers with low abundance were preferably placed here (48).

In this project, central markers for hypoxia, such as HIF1 alpha and VEGFA was prioritized, together with EMT markers and lineage specific cell markers. ECM markers, such as laminin and collagen type I were incorporated into the panel. Two separate panels were designed. The first panel for the original patient derived organoid model (Sachs *et al*.), and a second panel including immune cell markers for use in combination with the explant culture method. The second panel can be used with an organoid model in development, where immune and other stromal cells will be preserved in the tissue.

The strategy for the development of the IMC panel in thesis was to; 1) test of current *in-house* CyTOF and Hyperion validated antibodies, 2) acquire, and test new Hyperion validated antibodies, and 3) conjugate the remaining panel specific *in-house* markers. Validation of all antibodies was conducted with the use of positive controls we had generated for this purpose.

The development of the IMC panel was extremely time consuming. Especially the validation and titration of the desired antibodies. First and foremost, the antibodies were validated by staining the tissue of interest and compared it to a positive control tissue. Although markers could be positive in our tissue even though the signal might be much higher in the positive control, this was considered for the titration. These test runs might have to be repeated up to several times for an accurate validation and titration. Three test runs of a highly multiplexed antibody-panel were performed for validation and titration, before the main experiment. Although, even more runs should be performed to get sufficient validation and optimal titration for all included antibodies.

5.2 Result discussion

5.2.1 Development of human airway organoid

Establishment of a patient derived lung tumor organoid model is an important and necessary step for a better understanding of cancer development and progression, as well as a model for testing the efficacy of experimental therapies.

In the culturing, two defined serum free differentiation media were used, bronchiolar- and alveolar medium. The difference between these is the addition of CHIR, a Wnt activator, in the alveolar differentiation medium. This addition is necessary because the alveolar-type cells poorly proliferate in *ex vivo* conditions. The Wnt activator have previously shown to promote alveolar differentiation (49). Culture of organoids in both differentiation mediums were successful, although, in general a better growth was observed in the bronchiolar differentiated medium. Furthermore, we observed a variation in survival time when compared to organoids grown in the two different media. For some of the derived organoids, the bronchiolar differentiation medium gave longer survival, however others had better survival in the alveolar differentiation medium. This could be due to the preference of the organoid initiating cells. Alveolar cells have been shown to display lower proliferation, compared to bronchiolar cells. Alveolar cells have also shown to have loss of function over time (50). Additionally, growth rates vary between organoids derived from the different patient tumors, and this was as expected based on characterization of them.

Only stage I and II tumor resection were supposed to be received for the establishment of a patient derived organoid model. This is because surgery is a standard treatment strategy for stage I and II patients. For stage III and IV patients, surgery is not a standard recommendation (14, 15). However, due to margin of error of clinical staging some patients get a new stage after the pathological staging.

5.2.2 Characterization of organoids compared to tumor of origin.

One of the objectives of this thesis was to establish patient derived organoids originating from a variation of malignant phenotypes to examine differences in success of establishment as well as the histoarchitecture.

Adenocarcinomas are classified by five different predominant patterns, lepidic-, papillary-, acinar-, micropapillary- and solid adenocarcinoma (16). Three of these is a focus of this thesis. Lepidic predominant adenocarcinomas consists of atypical type II pneumocytes or Clara cells with malignant growth along normal structures, such as the alveoli (51). Papillary adenocarcinoma are defined as adenocarcinomas with over 75% of papillary structures supported by fibrovascular cores replacing the alveolar architecture (52). Acinar adenocarcinomas are characterized with round to oval glandular structures with luminal spaces surrounded by malignant cells (53). The squamous cell carcinomas are divided into keratinizing- and non-keratinizing squamous cell carcinoma. Typical markers of this malignancy are p40, CK5, CK6 and p63 (TRP63) (16).

In diagnosis of NSCLC, growth patterns and characteristics are assessed. To be able to separate adenocarcinomas from squamous cell carcinomas, the pathologist often applies AB-PAS histochemistry or IHC-P stain of tumor specimen tissue sections due to similar growth patterns. The two are often inseparable assessed from nuclear pleomorphism. Therefore, the AB-PAS stain of derived organoids was performed, to ease the comparison between organoids and patient tumor. As expected, organoids derived from adenocarcinomas displayed a higher secretion of mucin in the AB-PAS stains compared to the squamous cell carcinoma derived organoids. Also, the cell of origin which for adenocarcinomas has not been firmly established. However, candidates believed to be the cell of origin is Clara cells and type II pneumocytes (54). The type II pneumocytes are mucin secreting. Furthermore, the lack of mucin secretion in the squamous cell carcinoma organoid, might be a sign of lack of normal type II pneumocytes, and as such serves as an argument that the protocol is well suited to preserve malignant cells on the expense of normal non-malignant cells in culture. Of note, some research has shown similar patterns of mucin secretion in both adenocarcinomas and squamous cell carcinomas (55), and thus mucin secretion alone cannot be applied to discriminate between the two.

Antibody staining could be used for deeper investigation of mucin secretion. Department of Pathology at Haukeland University hospital uses two double stains for separation between adenocarcinoma and squamous cell carcinoma in the clinic. These are; TTF1 and NepsinA for adenocarcinoma and p40 and K5/6 for squamous cell carcinoma. These were performed when the pathologist deemed it necessary.

The addition of the IHC-P staining would also be useful to see if organoids preserve the typically characteristics of tumor derived from. These stains should be done, for further investigation of organoids characteristics and evaluation of their heterogeneity in cultures.

Patient derived organoids from adenocarcinomas have in general less compact structure compared to the squamous cell carcinoma derived organoids, resembling the *in vivo* growth pattern. Organoid size seems to vary between the tumor of origin rather than between adenocarcinoma and squamous cell carcinoma. Though, the size of the organoids rarely exceeded 200 µm in diameter in our experiment. For the less aggressive lung adenocarcinomas, this could be due to the limitation of alveoli size, which have an average size around 200 µm in diameter (56). For others the availability of oxygen and nutrients in the compact structures could serve to limit their growth. Prominent characteristics from patient tumor was preserved in derived organoids, such as the palisade formation in L6 (Figure 4.13 and 4.14). Organoids derived from tumors with prominent necrosis seems to have preserved necrotic areas (Figure 4.13), and this could be particularly useful for future studies of hypoxic microenvironment and hyperoxia as a therapeutic avenue. Furthermore, all derived organoids have relatively high expression of Ki67 as anticipated by the literature (57).

Finally, next generation sequencing (NGS) was performed on all adenocarcinomas, to investigate positive incidence of mutations. The respective derived organoids were stained with antibody. Unfortunately for the project, only one of the received patient adenocarcinoma tumors (L3) was positive for genetic alterations. The NGS of L3 tumor detected EGFR mutation in chromosome 19. EGFR mutation is the most common genetic mutation in NSCLC, with around 10% positive cases in Norway (58). Immunofluorescent antibody staining to detect EGFR chromosome 19 deletion were performed. The EGFR chromosome 19 deletion found by NGS in the patient tumor were confirmed in the organoids by positive staining (Figure 4.8) This result confirms that the patient derived organoids preserved also the genetic aberrations from the tumors they derive from, as expected according to the literature (43).

A challenge with the patient derived tumor models is the preservation of the malignant cells. The HE-stains indicates that, for most of the derived organoids, the cancer cells are preserved on the expense of normal cells in the culture. However, some of the L5 organoids looked more like normal lung organoids, while most resembles the micropapillary features of the tumor of origin. Ultimately, preservation of malignant cells in organoids on the expense of normal cells needs further investigation. One strategy could be to use the NGS results. Positive findings in the targeted NGS could make exclusion of growth factors in the medium recipe possible and thus promote growth of the cancer cells only, in the organoid cultures.

Thus, in conclusion we have shown that the characteristics of different PDO cultures differ from patient to patient, as one would expect, due to heterogeneity and lung cancer subtype. However, most importantly, the PDO´s show largely similar characteristics to the lung tumor of origin. This attribute makes patient 3D organoids applicable for clarification of treatment strategy for the individual patient, as shown by several researchers (59-61).

5.2.3 The effect of normobaric and hyperbaric oxygen treatment on patient derived organoids

Since hypoxia is a key factor in tumor growth and progression, our aim was also to evaluate the effect of hyperoxia (“the flip of the coin”) on lung tumors. To the best of our knowledge, this has not been done before.

Thus, elevated oxygen treatment, normobaric and hyperbaric, was performed on three of the organoid cultures, namely L1, L2, and L3.

Of note, we observed less organoids in the treated groups compared to control group which might indicate a growth inhibition due to the elevated oxygen. This correlates to *in vivo* studies on breast cancer after normobaric and hyperbaric oxygen treatment (62, 63). Ki67, a cell proliferation marker expressed in all active cell cycling phases, but not in the inactive phase (64), was stained by IF. This cell cycle phase- marker is associated with poor prognosis and cancer proliferation (65). Furthermore, Ki67 is induced by hypoxia, and has previously been

found to have high expression in hypoxic conditions (66, 67). Thus, we elucidated if enhanced oxygen would reduce this marker. However, only the normobaric treated showed significant reduction in Ki67. The hyperbaric treated however showed various results. Especially, in L2, where the organoids treated with normobaric oxygen show no expression of the proliferation marker Ki67. We cannot rule out that this could be due to staining error. Only L3 showed reduction of Ki67 staining under HBOT. However, the variable results could also reflect inter-person variability, and these experiments need to be performed again in order to be able to draw any firm conclusions. In the interest of time, since establishing the organoid cultures and embedding and sectioning them is a time-consuming process, we only got the opportunity to evaluate the effect of normobaric and hyperbaric oxygen therapy in L1, L2, and L3. From what we later learnt from histological examination, these were not the most hypoxic specimens out of the six tumors we established cultures from, and thus not the ones most likely to benefit from the normobaric and hyperbaric oxygen therapy. Thus, when repeating these experiments, we will use the organoids that show most severe hypoxia in patient tissues as well as organoid tissues, as we hypothesize that these will benefit most from the elevated oxygen therapy. Hyperbaric oxygen therapy could also be evaluated as personal treatment, and we conclude that the organoid models could be a suitable platform to test the efficacy of treatment and aid in the further development of this experimental therapy for individualized treatment regimens.

5.2.4 Imaging Mass Cytometry Results

We wanted to further investigate the histoarchitecture of the patient derived organoids, by conducting an experiment with the single cell high dimensional analysis technique, imaging mass cytometry.

The results show that there are some differences in the cellular compositions of organoids derived from adenocarcinomas compared to from squamous cell carcinomas.

Firstly, CK7 are only expressed in the adenocarcinoma derived organoid, this was expected. CK7 are expressed in almost all adenocarcinoma cases, and rarely expressed in squamous cell carcinomas (68). CK7 are often used as a marker to distinguish the two types (69).

Secondly, two markers for EMP were included in the IMC results, these were, E-cadherin and vimentin. However, both E-cadherin and vimentin are expressed in the adenocarcinoma derived organoids, while only E-cadherin and not vimentin are expressed in the squamous cell carcinoma derived organoids. Both of these markers are expected to be expressed in both types. Thus, vimentin is expected to have higher expression in adenocarcinomas (70).

5.3 Conclusions

Aim 1: Establish an organoid model from human non-small cell lung cancer resection specimens.

We managed to establish patient derived organoid cultures from a variety of different subtypes of NSCLC, four lung adenocarcinomas and two lung squamous cell carcinomas. We conclude that this was a relatively manageable procedure with a 100% success rate in this project.

With the added advantage of two individual differentiation media, the model is well suited for a wide range of future research purposes. Additionally, the procedure can be applicable for culturing of both normal and malignant lung tissue organoids from the same patient which is a great advantage for future application in cancer research *e.g.,* for drug efficacy and toxicity testing of novel anti-cancer compounds and treatment modalities.

Aim 2: Characterize the histoarchitecture and cellular composition of the organoids compared to the malignant tumors they derive from.

The patient derived organoids, form the different types of NSCLC, largely resemble the tumor of origin. The organoid cultures were determined to be heterogenous as expected due to the different types of NSCLC. And we were able to show that the 3D derived organoids in culture have preserved the histoarchitecture, and genetic mutations from the tumor they derived from were preserved. Additionally, the model was proven to obtain the functional ability of adenocarcinomas for mucin secretion, as determined by AB-PAS histochemistry.

We conclude that similar growth characteristics and histology between derived organoids and tumor of origin makes this model very applicable for personalized medicine.

Aim 3: Explore the effect of normobaric and hyperbaric oxygen treatment on cancer cell proliferation and phenotype, as well as ECM composition.

There seems to be less success in harvesting of organoids in the elevated oxygen treatment groups. Thus, these experiments need to be repeated with readouts on organoid number and size, as well as a live-dead marker included.

Our results indicate that elevated oxygen treatment influenced the cancer cell proliferation, as evidenced by less tissue. The normobaric oxygen treatment downregulates the proliferation marker Ki67, as one might expect, while the hyperbaric oxygen treatment showed variable results. Thus, these experiments should be repeated, and the most hypoxic organoid cultures should also be tested.

Thus, due to the preliminary nature of the results, we cannot conclude firmly whether or not elevated oxygen therapy is a promising therapeutic alternative for NSCLC, but our results support future exploration of this experimental therapy in the NSCLC organoid model established and characterized in this master project.

6. Future Perspectives

Taking the severity of lung cancer into consideration it is an important step to develop models more representative to the clinical cancer. This is important both for understanding the malignancies and the progressive tumor development and for the search for new therapeutic strategies.

The 3D patient derived organoid model established in this thesis show promising results with respect to preservation of histoarchitecture, functional characteristics and preservation of genetic mutations from patient tumors. Furthermore, we have shown that such a model is well suited in combination with single cell high dimension analysis, and especially IMC which also gives detailed spatial information. To this day, not enough is known regarding the detailed impact of hypoxia on the tumor microenvironment. This thesis has shown that the organoid model is a good starting point on future research on hypoxias effect on the tumor microenvironment, to get a better understanding of the complex communication between cancer cells and stromal cells. The combination of these two techniques is well suited for research in the area of precision medicine.

First of all, further analysis of the already acquired IMC data is to be performed. Due to unplanned service of the Hyperion imaging system, we did not have the time to complete the analyzation. Validation of HIF1 alpha in addition to VEGFA, for experiments on treated organoids could give a better conclusion on the effect of the elevated oxygen treatment. Furthermore, the addition of the antibodies used at the Department of pathology; p40 and K5/6 – adenocarcinoma and TTF1 and NepsinA – squamous cell carcinoma to the IMC panel would be an ideal next step for the panel design. In addition to the hypoxia markers in our panel, we want to add the hypoxia probe, pimonidazole, a 2-nitroimidazole, which is directly correlated with the level of hypoxia (71).

Our group have also started the development of a patient derived organoid model with the preservation of immune cells. A name for this new model is not yet decided, but it is either going to be called “organotypic spheroids” or “patient derived explant cultures”. The longevity of a such a model is short compared to this model, but it could be around two weeks to one month before the decrease of the immune cells. The addition of this new organoid model with

the preservation of immune as well as other stromal cells are also interesting for future studies, even though these have a shorter longevity compared to the model developed in this project where mainly malignant epithelial cells are preserved and expanded. However, the preservation of these immune and stromal cell will be even more representative of the cancer *in situ* with components of the complex tumor immune microenvironment present. Thus, this "patient derived explant culture" model is well suited for the elevated oxygen treatment model and will complement the model established here very well. Possible complications with the hyperbaric oxygen treatment on lung cancer patients, makes it more reasonable to introduce the normobaric treatment strategy on lung cancer patients, which gave promising results in this project.

7. References

1. Organization WH. World Health Organization. Global cancer data. Int Agency Res cancer 2021 [Available from: https://www.who.int/news-room/fact-sheets/detail/cancer.
2. Bray F, Ferlay J, Soerjomataram I, Siegel RL, Torre LA, Jemal A. Global cancer statistics 2018: GLOBOCAN estimates of incidence and mortality worldwide for 36 cancers in 185 countries. CA Cancer J Clin. 2018;68(6):394-424.
3. FHI. Cause of Death, Norway.
4. WHO. Globocan. 2020.
5. Siegel RL, Miller KD, Jemal A. Cancer statistics, 2019. CA Cancer J Clin. 2019;69(1):7-34.
6. Wong MCS, Lao XQ, Ho KF, Goggins WB, Tse SLA. Incidence and mortality of lung cancer: global trends and association with socioeconomic status. Sci Rep. 2017;7(1):14300.
7. Yu Y, Luo Y, Zheng Y, Zheng X, Li W, Yang L, et al. Exploring the mechanism of non-small-cell lung cancer cell lines resistant to epidermal growth factor receptor tyrosine kinase inhibitor. J Cancer Res Ther. 2016;12(1):121-5.
8. Oronsky B, Reid TR, Oronsky A, Carter CA. What's New in SCLC? A Review. Neoplasia. 2017;19(10):842-7.
9. Lemjabbar-Alaoui H, Hassan OU, Yang YW, Buchanan P. Lung cancer: Biology and treatment options. Biochim Biophys Acta. 2015;1856(2):189-210.
10. Hanna JM, Onaitis MW. Cell of origin of lung cancer. J Carcinog. 2013;12:6.
11. Detterbeck FC, Boffa DJ, Tanoue LT. The new lung cancer staging system. Chest. 2009;136(1):260-71.
12. Woodard GA, Jones KD, Jablons DM. Lung Cancer Staging and Prognosis. Cancer Treat Res. 2016;170:47-75.
13. team TACSmaec. Non-Small Cell Lung Cancer Stages. Cancerorg. 2019.
14. Zarogoulidis K, Zarogoulidis P, Darwiche K, Boutsikou E, Machairiotis N, Tsakiridis K, et al. Treatment of non-small cell lung cancer (NSCLC). J Thorac Dis. 2013;5 Suppl 4:S389-96.
15. lungekreftgruppe N. Lungekreft, mesoteliom og thymom Retningslinjer for utredning og behandling.
16. Inamura K. Lung Cancer: Understanding Its Molecular Pathology and the 2015 WHO Classification. Front Oncol. 2017;7:193.

17. Santos GdC, Shepherd FA, Tsao MS. EGFR Mutations and Lung Cancer. Annual Review of Pathology: Mechanisms of Disease. 2011;6(1):49-69.
18. Sculier JP, Berghmans T, Meert AP. Advances in target therapy in lung cancer. Eur Respir Rev. 2015;24(135):23-9.
19. Hashemi-Sadraei N, Hanna N. Targeting FGFR in Squamous Cell Carcinoma of the Lung. Target Oncol. 2017;12(6):741-55.
20. Meseure KDAaD. Significance of Tumor Microenvironment Scoring and Immune Biomarkers in Patient Stratification and Cancer Outcomes. 2018.
21. Padhi A, Nain AS. ECM in Differentiation: A Review of Matrix Structure, Composition and Mechanical Properties. Ann Biomed Eng. 2020;48(3):1071-89.
22. Estrella V, Chen T, Lloyd M, Wojtkowiak J, Cornnell HH, Ibrahim-Hashim A, et al. Acidity generated by the tumor microenvironment drives local invasion. Cancer Res. 2013;73(5):1524-35.
23. Byrne MB, Leslie MT, Gaskins HR, Kenis PJA. Methods to study the tumor microenvironment under controlled oxygen conditions. Trends Biotechnol. 2014;32(11):556-63.
24. Terry S, Engelsen AST, Buart S, Elsayed WS, Venkatesh GH, Chouaib S. Hypoxia-driven intratumor heterogeneity and immune evasion. Cancer Lett. 2020;492:1-10.
25. Michieli P. Hypoxia, angiogenesis and cancer therapy: to breathe or not to breathe? Cell Cycle. 2009;8(20):3291-6.
26. Harris AL. Hypoxia--a key regulatory factor in tumour growth. Nat Rev Cancer. 2002;2(1):38-47.
27. Moen I, Stuhr LE. Hyperbaric oxygen therapy and cancer--a review. Target Oncol. 2012;7(4):233-42.
28. Holmquist L, Lofstedt T, Pahlman S. Effect of hypoxia on the tumor phenotype: the neuroblastoma and breast cancer models. Adv Exp Med Biol. 2006;587:179-93.
29. Cannito S, Novo E, Compagnone A, Valfre di Bonzo L, Busletta C, Zamara E, et al. Redox mechanisms switch on hypoxia-dependent epithelial-mesenchymal transition in cancer cells. Carcinogenesis. 2008;29(12):2267-78.
30. Xingbo Xu XT, BjörnTampe, Elisa Sanchez Michael Zeisberg and Elisabeth M.Zeisberg. Snail Is a Direct Target of Hypoxia-inducible Factor 1α (HIF1α) in Hypoxia-induced Endothelial to Mesenchymal Transition of Human Coronary Endothelial Cells. Journal of Biological Chemistry. 2015;290(27).

31. Xu FX, Zhang YL, Liu JJ, Zhang DD, Chen HB. Hypoxic markers in non-small cell lung cancer (NSCLC) - A review. Eur Rev Med Pharmacol Sci. 2016;20(5):849-52.
32. Joseph JP, Harishankar MK, Pillai AA, Devi A. Hypoxia induced EMT: A review on the mechanism of tumor progression and metastasis in OSCC. Oral Oncol. 2018;80:23-32.
33. Jr FMaDJJ. Cancer and the tumor microenvironment: a review of an essential relationship. Cancer Chemother Pharmacol. 2009.
34. Tam WL, Weinberg RA. The epigenetics of epithelial-mesenchymal plasticity in cancer. Nat Med. 2013;19(11):1438-49.
35. Brabletz T, Kalluri R, Nieto MA, Weinberg RA. EMT in cancer. Nat Rev Cancer. 2018;18(2):128-34.
36. Yilmaz M, Christofori G. EMT, the cytoskeleton, and cancer cell invasion. Cancer Metastasis Rev. 2009;28(1-2):15-33.
37. Loh CY, Chai JY, Tang TF, Wong WF, Sethi G, Shanmugam MK, et al. The E-Cadherin and N-Cadherin Switch in Epithelial-to-Mesenchymal Transition: Signaling, Therapeutic Implications, and Challenges. Cells. 2019;8(10).
38. Nagle PW, Plukker JTM, Muijs CT, van Luijk P, Coppes RP. Patient-derived tumor organoids for prediction of cancer treatment response. Semin Cancer Biol. 2018;53:258-64.
39. Sachs N, Papaspyropoulos A, Zomer-van Ommen DD, Heo I, Bottinger L, Klay D, et al. Long-term expanding human airway organoids for disease modeling. EMBO J. 2019;38(4).
40. Senior W. Staining of animal tissues with the dye base of methylene green in benzene to facilitate identification and selection of material. Stain Technol. 1969;44(6):269-71.
41. Schindelin JA-C, I. & Frise, E. et al. Fiji: an open-source platform for biological-image analysis. Nature methods. 2012.
42. Kamentsky L JT, Fraser A, Bray M, Logan D, Madden K, Ljosa V, Rueden C, Harris GB, Eliceiri K, Carpenter AE. Improved structure, function, and compatibility for CellProfiler: modular high-throughput image analysis software. Bioinformatics. 2011.
43. Kim M, Mun H, Sung CO, Cho EJ, Jeon H-J, Chun S-M, et al. Patient-derived lung cancer organoids as in vitro cancer models for therapeutic screening. Nature Communications. 2019;10(1):3991.
44. Foley KE. Organoids: a better in vitro model. Nat Methods. 2017;14(6):559-62.
45. Fluidigm. Imaging Mass Cytometry.

46. Baharlou H, Canete NP, Cunningham AL, Harman AN, Patrick E. Mass Cytometry Imaging for the Study of Human Diseases-Applications and Data Analysis Strategies. Front Immunol. 2019;10:2657.
47. Elaldi R, Hemon P, Petti L, Cosson E, Desrues B, Sudaka A, et al. High Dimensional Imaging Mass Cytometry Panel to Visualize the Tumor Immune Microenvironment Contexture. Front Immunol. 2021;12:666233.
48. Fluidigm. Guidelines for Mass Cytometry Panel Design.
49. al AJe. Differentiation of Human Pluripotent Stem Cells into Functional Lung Alveolar Epithelial Cells
. Cell Stem Cell. 2017.
50. Kim JH, An GH, Kim JY, Rasaei R, Kim WJ, Jin X, et al. Human pluripotent stem-cell-derived alveolar organoids for modeling pulmonary fibrosis and drug testing. Cell Death Discov. 2021;7(1):48.
51. Duruisseaux M, Antoine M, Rabbe N, Rodenas A, Mc Leer-Florin A, Lacave R, et al. Lepidic predominant adenocarcinoma and invasive mucinous adenocarcinoma of the lung exhibit specific mucin expression in relation with oncogenic drivers. Lung Cancer. 2017;109:92-100.
52. Karmakar S, Nath A, Neyaz Z, Agarwal V, Ahsan S. Primary papillary adenocarcinoma of the lung: Report of two cases. Lung India. 2017;34(3):299-302.
53. Kadota K, Yeh YC, Sima CS, Rusch VW, Moreira AL, Adusumilli PS, et al. The cribriform pattern identifies a subset of acinar predominant tumors with poor prognosis in patients with stage I lung adenocarcinoma: a conceptual proposal to classify cribriform predominant tumors as a distinct histologic subtype. Mod Pathol. 2014;27(5):690-700.
54. Tomoya Fukui RS, Francisco Agosto-Perez, Jason G. Mezey, Robert J. Downey, William D. Travis, Ronald G. Crystal. Lung adenocarcinoma subtypes based on expression of human airway basal cell genes. European Respiratory journal. 2013.
55. Lakshmanan I, Ponnusamy MP, Macha MA, Haridas D, Majhi PD, Kaur S, et al. Mucins in lung cancer: diagnostic, prognostic, and therapeutic implications. J Thorac Oncol. 2015;10(1):19-27.
56. Ochs M, Nyengaard JR, Jung A, Knudsen L, Voigt M, Wahlers T, et al. The number of alveoli in the human lung. Am J Respir Crit Care Med. 2004;169(1):120-4.
57. Del Gobbo A, Pellegrinelli A, Gaudioso G, Castellani M, Zito Marino F, Franco R, et al. Analysis of NSCLC tumour heterogeneity, proliferative and 18F-FDG PET indices reveals Ki67 prognostic role in adenocarcinomas. Histopathology. 2016;68(5):746-51.

58. Helsedirektoratet. Nasjonalt handlingsprogram med retningslinjer for diagnostikk, behandling og oppfølging av lungekreft, mesoteliom og thymom 2021.
59. Wensink GE, Elias SG, Mullenders J, Koopman M, Boj SF, Kranenburg OW, et al. Patient-derived organoids as a predictive biomarker for treatment response in cancer patients. npj Precision Oncology. 2021;5(1):30.
60. Nero C, Vizzielli G, Lorusso D, Cesari E, Daniele G, Loverro M, et al. Patient-derived organoids and high grade serous ovarian cancer: from disease modeling to personalized medicine. J Exp Clin Cancer Res. 2021;40(1):116.
61. Vlachogiannis G, Hedayat S, Vatsiou A, Jamin Y, Fernandez-Mateos J, Khan K, et al. Patient-derived organoids model treatment response of metastatic gastrointestinal cancers. Science. 2018;359(6378):920-6.
62. Yttersian Sletta K, Tveitaras MK, Lu N, Engelsen AST, Reed RK, Garmann-Johnsen A, et al. Oxygen-dependent regulation of tumor growth and metastasis in human breast cancer xenografts. PLoS One. 2017;12(8):e0183254.
63. Smeland HY, Lu N, Karlsen TV, Salvesen G, Reed RK, Stuhr L. Stromal integrin alpha11-deficiency reduces interstitial fluid pressure and perturbs collagen structure in triple-negative breast xenograft tumors. BMC Cancer. 2019;19(1):234.
64. Scholzen T, Gerdes J. The Ki-67 protein: From the known and the unknown. Journal of Cellular Physiology. 2000;182(3):311-22.
65. Li LT, Jiang G, Chen Q, Zheng JN. Ki67 is a promising molecular target in the diagnosis of cancer (Review). Mol Med Rep. 2015;11(3):1566-72.
66. Zhang L, Hu Y, Xi N, Song J, Huang W, Song S, et al. Partial Oxygen Pressure Affects the Expression of Prognostic Biomarkers HIF-1 Alpha, Ki67, and CK20 in the Microenvironment of Colorectal Cancer Tissue. Oxid Med Cell Longev. 2016;2016:1204715.
67. L. Xiang Z-HL, Q. Huan et al. Hypoxia-inducible factor-2a is associated with ABCG2 expression, histology-grade and Ki67 expression in breast invasive ductal carcinoma. Diagnostic Pathology. 2012;vol 7.
68. Gurda GT, Zhang L, Wang Y, Chen L, Geddes S, Cho WC, et al. Utility of five commonly used immunohistochemical markers TTF-1, Napsin A, CK7, CK5/6 and P63 in primary and metastatic adenocarcinoma and squamous cell carcinoma of the lung: a retrospective study of 246 fine needle aspiration cases. Clinical and Translational Medicine. 2015;4(1):16.
69. Xu XY, Yang GY, Yang JH, Li J. Analysis of clinical characteristics and differential diagnosis of the lung biopsy specimens in 99 adenocarcinoma cases and 111 squamous cell

carcinoma cases: utility of an immunohistochemical panel containing CK5/6, CK34betaE12, p63, CK7 and TTF-1. Pathol Res Pract. 2014;210(10):680-5.
70. Prudkin L, Liu DD, Ozburn NC, Sun M, Behrens C, Tang X, et al. Epithelial-to-mesenchymal transition in the development and progression of adenocarcinoma and squamous cell carcinoma of the lung. Mod Pathol. 2009;22(5):668-78.
71. Aguilera KY, Brekken RA. Hypoxia Studies with Pimonidazole in vivo. Bio Protoc. 2014;4(19).

8. Appendix

CellProfiler pipelines: https://tjinfo.uib.no/vedlegg